Journal of Computational Physics 498 (2024) 112665

Contents lists available at ScienceDirect

Journal of Computational Physics

journal homepage: www.elsevier.com/locate/jcp

An optimization-based discrete element model for dry granular flows: Application to granular collapse on erodible beds

Hugo A. Martin [a,b,*], Anne Mangeney [a,c], Aline Lefebvre-Lepot [d], Bertrand Maury [e,f], Yvon Maday [b,c]

[a] Université Paris Cité, Institut de physique du globe de Paris, CNRS, F-75005 Paris, France
[b] Sorbonne Université, CNRS, Université Paris Cité, Laboratoire Jacques-Louis Lions (LJLL), F-75005 Paris, France
[c] Institut Universitaire de France (IUF), 75231 Paris Cedex 05, France
[d] CMAP, CNRS, École Polytechnique, Institut Polytechnique de Paris, 91128 Palaiseau Cedex, France
[e] Département de Mathématiques Appliquées, École Normale Supérieure, Université PSL, 75005 Paris, France
[f] Laboratoire de Mathématiques d'Orsay, Université Paris-Saclay, 91405 Orsay Cedex, France

ARTICLE INFO

Keywords:
Discrete element methods
Convex methods
Contact dynamics
Erodible bed
Granular media
Erosion waves

ABSTRACT

Erosion processes and the associated static/flowing transition in granular flows are still poorly understood despite their crucial role in natural hazards such as landslides and debris flows. Continuum models do not yet adequately reproduce the observed increase of runout distance of granular flows on erodible beds or the development of waves at the bed/flow interface. Discrete Element Methods, which simulate each grain's motion and their complex interactions, provide a unique tool to investigate these processes numerically. Among them, Convex Methods (CM), resulting from the convexification of Contact Dynamics methods, benefit from a robust theoretical framework, ensuring the convergence of the numerical solution at every time iteration. They are also intrinsically more stable than classical Molecular Dynamics methods. However, although already implemented in engineering fields, CMs have not yet been tested in the framework of flows on erodible beds. We present here a Convex Optimization Contact Dynamics (COCD) method and prove that it generates a numerical solution verifying Coulomb's law at each contact and iteration. After its calibration and validation with experiments and another widely used Contact Dynamics method, we show that our simulations accurately reproduce qualitative and even many quantitative characteristics of experimental granular flows on erodible beds, including the increase of runout distance with the thickness of the erodible bed, the change of the static/flowing interface and the presence of erosion waves behind the flow front. Beyond erosion processes, our article endorses CMs as potential accurate tools for exploring complex granular mechanisms.

1. Introduction

Granular materials are involved in numerous geophysical flows such as landslides, debris flows, debris and snow avalanches, pyroclastic flows and rockfalls on Earth and other planetary bodies [1–7]. These events represent major natural hazards threatening

* Corresponding author.
E-mail address: martin_hugo@ymail.com (H.A. Martin).

https://doi.org/10.1016/j.jcp.2023.112665
Received 28 September 2022; Received in revised form 16 November 2023; Accepted 20 November 2023

Available online 23 November 2023

populations and infrastructures, especially in mountainous, coastal, volcanic and seismic areas. The risks associated with landslides and potential generated tsunamis increase with increasing human population and activity and with increasing severity and frequency of rainfall events related to climate change [8,6,9]. These flows occur on steep to gentle slopes and involve complex physical processes such as the presence of a fluid phase, heterogeneous materials, fragmentation and segregation effects, and erosion/deposition processes [10,11,1,12–14]. The lack of understanding of these processes questions physics-based hazard assessment for these geophysical flows that present a high mobility that is still an open issue despite increasing research on this topic [2,15].

A huge amount of work has been performed these last thirty years on granular flows, spanning laboratory experiments, numerical modeling and field observation. As pointed out above, a full understanding of the physical processes involved in these flows is still however lacking, even for simple laboratory-scale granular flows. At the particle scale, complex interactions between grains involving nonlinear friction forces and inelastic collisions are involved. There are also geometrical constraints on a granular material for which the density can typically vary from those of crystal-like static configurations to those of gas-like flows [16].

Multiple modeling strategies have been proposed to simulate granular materials. A first approach is based on continuum macroscopic models solving the full Navier-Stokes like equations [17–21] or the simplified thin-layer (i.e., shallow-water) equations [22–28]. The second class of approaches, namely Discrete Elements Methods (DEM), relies on a microscopic description of the medium. In DEM, the granular material is considered as an assembly of rigid grains. In DEM, the models are based on variables defined at the scale of individual particles. These variables are typically the positions/velocities of the grains and contact forces. When considering these methods, the difficult task is to compute the interactions between the particles. This computation can be done using different approaches, identified as “soft” and “hard” methods. In the past thirty years, the number of studies involving DEM, especially the “soft” formulation, has considerably increased in all domains of application, in particular for flows at the laboratory scale [29–32].

The first discrete element method to model the contacts between grains was the so-called Molecular Dynamics (MD) method. It dates back to 1979 with the work of Cundall and Strack [33]. For real grains, the contact forces are modeled with Hertz’s law of contact through functions depending on the elastic particle’s deformation at the contact. In MD, the contact forces are functions parameterized by the numerical overlap between the grains during the contact (see Ref. [34] for a detailed description). MD is a “soft” discrete method in the sense that grains are considered as slightly deformable, so that contact forces are differentiable. MD is quite efficient in many situations and various refined contact force models have been developed. It makes it possible to reproduce a wide range of contact phenomena (see, e.g., Ref. [35] for a list of about 40 possible contact models).

However, from a numerical point of view, the time discretization in MD is based on an explicit scheme, raising stability issues because of the stiffness of the interaction forces. More precisely, to maintain numerical stability, the time step used must be very small. In many situations, this makes it necessary to artificially decrease the rigidity of grains [36]. As a consequence, it is difficult to reproduce static configurations, even when adding artificial dissipation terms. Note also that the acoustic phenomena that appear in actual MD computations do not correspond in general to realistic wave propagation phenomena because of this artificial decrease of grain rigidity [36].

The first discrete method that can be qualified as “hard” was the so-called Contact Dynamics (CD) method, developed by Moreau and Jean in the 1990s. Contrary to MD, the contact forces are not modeled explicitly with functions, but instead they are implicit and are required to satisfy contact laws, which typically express inelastic collisions together with friction. We refer to the seminal works [37–43] for a detailed description of this approach. Contrary to MD, CD leads to contact forces that are not bounded in time since they are not functions of time but rather impulses satisfying contact laws. The computational cost at each time steps is usually more than in MD. However implicit schemes can be used, which makes it possible to use large time steps while still ensuring stability.

In CD, for systems with contact laws that express non-overlapping and frictional phenomena (Coulomb’s law), the equations of motion can be written as a combination of Newton’s second law with dynamic and kinematic constraints. A straight time-discretization of the problem leads to a non-convex Linear Complementarity Problem (LCP) (see, e.g., Refs. [44,45]), which is expensive to solve. The most widely spread numerical strategies to deal with the friction cone constraint are projection/splitting methods, Gauss-Seidel like relaxations, or generalized Newton methods (see Ref. [46] for a review of these methods). Unfortunately, no convergence results for the corresponding iterative methods are available. Among these methods, the Non-Smooth Contact Dynamics (NSCD) method [42,47] has encountered significant success, especially for comparisons with experiments (see Refs. [48,49]).

In Ref. [50], the authors proposed another approach to compute an approximate solution to the LCP. This strategy consists in solving a fixed-point problem, iterating on parameterized convex optimization problems that are proved to converge toward the LCP’s solution at each time step. At each step of the fixed-point algorithm, it is required to solve a conic minimization problem.

The last approach we consider here is based on a convexification of the non-overlapping constraint, in line with Refs. [51,52]. We refer to these approaches as Convexified Methods (CM). From this convexification, the time sub-problem obtained can be turned into a conic constrained optimization problem. Therefore, it makes it possible to use existing and convergent solvers to compute the solution at each time step. From a numerical point of view, several approaches solve the corresponding Cone Complementarity Problem (CCP) [51–55], while our strategy is to take advantage of the minimization problem. This minimization problem can be based on the global force vector as the unknown; see Refs. [56–61]. A short review of the different numerical methods introduced above is presented in Sec. 2.2 and solver efficiencies are compared in Ref. [60]. From a theoretical point of view, all these studies systematically refer to Refs. [51,52]. In the first one some theoretical developments are proposed in the case of a facet discretization of the Coulomb friction cone. In the second one, in the framework of the full circular Coulomb cone, the authors reinterpret the scheme in terms of a minimization problem based on the forces.

In this article, we consider the dual formulation of the optimization problem, based on using the global velocity vector as the unknown [62] together with the full circular Coulomb cone. In the following, we will refer to the method presented in this article

as Convex Optimization Contact Dynamics (COCD). It is a convexified velocity-based CM formulation. Let us describe its main properties:

- The conditions verified by the optimal solution of the minimization problem are rigorously proved in the framework of convex analysis. We show that they take the form of a discretization of the continuous problem, with the Coulomb's law verified at every contact and at every time step. The error in the local Coulomb's law scales like the precision of the optimization solver.
- This method is known to artificially push apart particles at the first order in time. Our validation tests show that this drawback has no effect on the ability of the scheme to properly reproduce the expected macroscopic behavior in the context of gravity-driven granular flows.
- Because of its optimization formulation, the numerical solution is ensured to converge at every time integration.
- Since the scheme is implicit, large time step values can be used.

In spite of the artificial gap mentioned above, which is common to all convexified methods (CM), we show the excellent behavior of such schemes by confronting COCD to multiple validation processes. Indeed, COCD is first validated through quantitative comparisons with simulations (with NSCD [48,49], in which the non-convex scheme is used) and with experimental results [63,64] in gravity-driven granular flows. In a second step, we use COCD to investigate how the presence of a basal erodible layer affects granular flows on top of it. To the authors' knowledge, it is the first article involving a CM in the framework of granular flows on erodible beds. The particle-scale processes involved in these erosion phenomena are still open questions for both laboratory- and field-scale granular flows, even though they are known to play a crucial role in landslides or avalanches [65,66,11,67–69,14,70,71].

Several laboratory experiments involving granular flows on erodible beds have been performed. The experimental setups implement, for example, releases of grains on a static erodible layer on horizontal or sloping beds [23,63,64,72] or constant inflows, leading to erosion-deposition waves [28,73,74]. In particular, laboratory-scale experiments of granular collapses showed that the presence of even a very thin layer of erodible particles can significantly increase the duration and the maximum distance (runout) reached by granular flows on slopes larger than about half of the characteristic friction angles of the granular material involved [63,64]. More precisely, there is no increase in the runout distance for horizontal planes, but there can be an increase of 40% for inclined planes. These articles also showed that the runout distance increases with increasing thickness of the erodible bed and with the slope angle. Even though the increase of runout distance has been qualitatively reproduced with continuum granular flow models with the $\mu(I)$-rheology [75–77], quantitative agreement is still quite poor. This raises the question as to whether particle-scale processes, not accounted for in classical continuum models, may be a promising element to better reproduce laboratory observations. As it is challenging to make such measurements even in laboratory-scale experiments, DEM simulations provide a unique tool to investigate these effects.

First 3D DEM simulations of granular flows on erodible beds lying on a horizontal plane showed that for granular columns with a relatively high initial aspect ratio ($a = H/D > 3$, where H and D are the column height and diameter, respectively), the runout distance is still observed to increase, as in experiments [78]. However, a deep insight into the comparison between DEM simulations and laboratory experiments is still lacking.

In this article, we show that COCD accurately reproduces complex behaviors observed in laboratory-scale experiments of granular flows on erodible beds. We complete the results of Ref. [78] with different inclination angles of the bed and different thicknesses of the erodible layer lying on top of it. Furthermore, COCD is quantitatively compared to granular collapse experiments performed by Mangeney et al. (2010) [63] and Farin et al. (2014) [64]. The increase in runout distance is found to be well reproduced by the model. In addition, the static/flowing transition within the granular media and its evolution inside the erodible layer are in very good agreement with observations. Finally, COCD surprisingly reproduces the "wave" behavior observed at the interface between the initially flowing and initially static grains [64]. All these comparisons show that such CD models contain the key physical ingredients to reproduce and thus gain insight into erosion processes in granular flows.

In Sec. 2, the continuous problem and its time discretization scheme COCD are described. The theoretical results are presented. In Sec. 3, we present a simple implementation of COCD using the MOSEK solver [79] and computational aspects such as the termination criteria and the solver tolerance according to time step values that help COCD to reproduce experiments. We also show that the method well reproduces the results obtained with the NSCD method. In Sec. 4, our method is compared to column collapse experiments leading to the calibration of COCD parameters. Finally, the application of COCD to granular flows on erodible beds is presented in Sec. 5.

2. Continuous problem and time discretization scheme

Let us consider a mechanical system in $\mathbb{R}^3$, composed of N rotational rigid spheres with given fixed radii $r_i > 0$ and masses $m_i > 0$, $i = 1, \dots, N$. The center of sphere i is denoted by $\boldsymbol{c}_i \in \mathbb{R}^3$, and its instantaneous velocity by $\boldsymbol{v}_i \in \mathbb{R}^3$. Since we consider spheres only, we shall not follow the orientation of bodies, and simply consider here the instantaneous rotation vector $\boldsymbol{\omega}_i \in \mathbb{R}^3$. We denote by

$$\boldsymbol{c} = (\boldsymbol{c}_1, \dots, \boldsymbol{c}_N) \in \mathbb{R}^{3N} \text{ and } \boldsymbol{u} = (\boldsymbol{v}_1, \boldsymbol{\omega}_1, \dots, \boldsymbol{v}_N, \boldsymbol{\omega}_N) \in \mathbb{R}^{6N}$$

the generalized position and velocity field vectors.

The signed distance between spheres i and j is defined by:

$$\mathrm{D}_{ij}(\boldsymbol{c}) = \left| \boldsymbol{c}_i - \boldsymbol{c}_j \right| - \left(r_i + r_j \right),$$

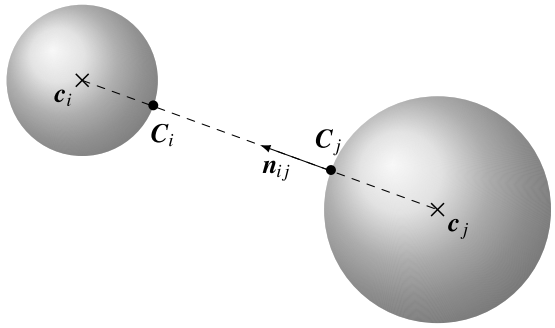

Fig. 1. Notations.

where $|\cdot|$ is the euclidean norm so that the non-overlapping condition writes $\mathrm{D}_{ij} \geq 0$.

For any two grains i and j, with centers $\boldsymbol{c}_i$ and $\boldsymbol{c}_j$, we denote by $\boldsymbol{C}_i$ and $\boldsymbol{C}_j$ the points which realize the distance (with $\boldsymbol{C}_i = \boldsymbol{C}_j$ if the spheres are in contact; see Fig. 1). We define the associated position vectors $\boldsymbol{r}_i = \boldsymbol{C}_i - \boldsymbol{c}_i$, $\boldsymbol{r}_j = \boldsymbol{C}_j - \boldsymbol{c}_j$.

We consider the normal direction to the surfaces of the particles at points $\boldsymbol{C}_i$ and $\boldsymbol{C}_j$, which is shared by the two particles. We introduce the unit vector $\boldsymbol{n}_{ij}$, defined as the corresponding normal vector pointing to particle i. Since we consider spherical particles, we have:

$$\boldsymbol{n}_{ij} = \frac{\boldsymbol{c}_i - \boldsymbol{c}_j}{|\boldsymbol{c}_i - \boldsymbol{c}_j|}.$$

We denote by $P_{ij}\boldsymbol{v} = \boldsymbol{v} - (\boldsymbol{v}\cdot\boldsymbol{n}_{ij})\boldsymbol{n}_{ij}$ the projection of $\boldsymbol{v}$ on Π_{ij}, the plane that is orthogonal to $\boldsymbol{n}_{ij}$ and thus parallel to the tangent planes in $\boldsymbol{C}_i$ and $\boldsymbol{C}_j$.

We also define A_{ij} as the linear operator which maps the generalized velocity field $\boldsymbol{u} \in \mathbb{R}^{6N}$ to the relative velocity between the points $\boldsymbol{C}_i$ and $\boldsymbol{C}_j$ at which the distance between spheres i and j is attained, i.e.

$$A_{ij}\boldsymbol{u} = \boldsymbol{v}_i + \boldsymbol{\omega}_i \wedge \boldsymbol{r}_i - (\boldsymbol{v}_j + \boldsymbol{\omega}_j \wedge \boldsymbol{r}_j) \in \mathbb{R}^3.$$

Straightforward computations show that for any generalized velocity $\boldsymbol{u} \in \mathbb{R}^{6N}$ and any vector $\boldsymbol{f} \in \mathbb{R}^3$, we have $A_{ij}\boldsymbol{u}\cdot\boldsymbol{f} = \boldsymbol{u}\cdot A_{ij}^T\boldsymbol{f}$ with

$$A_{ij}^T\boldsymbol{f} = (\boldsymbol{0},\dots,\boldsymbol{0},\ \underbrace{\boldsymbol{f},\boldsymbol{r}_i\wedge\boldsymbol{f}}_{\text{position } i},\boldsymbol{0},\dots,\boldsymbol{0},\ \underbrace{-\boldsymbol{f},-\boldsymbol{r}_j\wedge\boldsymbol{f}}_{\text{position } j},\boldsymbol{0},\dots,\boldsymbol{0}) \in \mathbb{R}^{6N},$$

so that A_{ij}^T maps a vector $\boldsymbol{f} \in \mathbb{R}^3$ to the generalized force/moment vector corresponding to the force $\boldsymbol{f}$ exerted on particle i at point $\boldsymbol{C}_i$ and the opposite force $-\boldsymbol{f}$ exerted on particle j at point $\boldsymbol{C}_j$.

The vector $P_{ij}A_{ij}\boldsymbol{u}$ represents the tangential relative velocity. As a consequence, when two spheres are in contact with no relative normal motion, i.e., $\boldsymbol{n}_{ij}\cdot A_{ij}\boldsymbol{u} = 0$, then $P_{ij}A_{ij}\boldsymbol{u} = 0$ expresses a rolling motion with no slip, while $P_{ij}A_{ij}\boldsymbol{u} \neq 0$ corresponds to a sliding motion.

At any time, we shall denote by I_c the set of all possible pairs of contacts: $I_c = \{(i,j)\ 1 \leq i < j \leq N\}$. Note the pair of grains i and j is represented only once in I_c through the couple (i,j) if $i<j$ and (j,i) if $j<i$.

We consider that no external torque is exerted on the grains. If $\boldsymbol{f}_i^{ext} \in \mathbb{R}^3$ is the external force exerted on particle i we define the generalized force vector as $\mathbf{f}^{ext} = (\boldsymbol{f}_1^{ext},0,\dots,\boldsymbol{f}_N^{ext},0) \in \mathbb{R}^{6N}$. We then define the $6N\times 6N$ generalized mass matrix (masses and moments of inertia) as

$$M = \mathrm{diag}\left(m_1,m_1,m_1,J_1,J_1,J_1,m_2,\dots,J_N,J_N,J_N\right).$$

The equations of motion write:

$$\mathrm{M}\frac{d\boldsymbol{u}}{dt} = \mathbf{f}^{ext} + \sum_{\alpha\in I_c} A_\alpha^T\left(f_n^\alpha\boldsymbol{n}_\alpha + \boldsymbol{f}_t^\alpha\right), \tag{1}$$

$$f_n^\alpha \geq 0,\ D_\alpha \geq 0,\ f_n^\alpha D_\alpha = 0 \quad \alpha\in I_c,$$

$$\text{If } D_\alpha(\boldsymbol{c}) = 0 \text{ then } (A_\alpha\boldsymbol{u}^+)\cdot\boldsymbol{n}_\alpha = 0 \quad \alpha\in I_c, \tag{2}$$

$$\text{If } P_\alpha A_\alpha\boldsymbol{u}^+ \neq 0 \text{ (sliding motion)},\ \boldsymbol{f}_t^\alpha = -\mu f_n^\alpha\frac{P_\alpha A_\alpha\boldsymbol{u}^+}{|P_\alpha A_\alpha\boldsymbol{u}^+|} \quad \alpha\in I_c, \tag{3}$$

$$\text{If } P_\alpha A_\alpha\boldsymbol{u}^+ = 0 \text{ (no slip)},\ |\boldsymbol{f}_t^\alpha| \leq \mu f_n^\alpha \quad \alpha\in I_c. \tag{4}$$

Note that the translational and rotational velocities are likely to be non-smooth, since they undergo instantaneous jumps during collision. In particular, the post-collision velocity $\boldsymbol{u}^+$ can be different from the pre-collision velocity $\boldsymbol{u}^-$. As a consequence, the evolution above is to be understood in a weak, distributional sense.

Let us add a few comments on the previous equations. For a pair of grains $\alpha = (i,j) \in I_c$, in contact, the corresponding vector $f_n^{ij}\boldsymbol{n}_{ij} + \boldsymbol{f}_t^{ij} \in \mathbb{R}^3$ is transmitted to both particles i and j through A_{ij}^T. Indeed, let us define

$$f_n^{ji} = f_n^{ij}, \quad \boldsymbol{f}_t^{ji} = -\boldsymbol{f}_t^{ij}, \quad \forall \alpha = (i,j) \in I_c.$$

Then, using the expression for A_{ij}^T, Equation (1) can be rewritten:

$$m_i \dot{\boldsymbol{v}}_i = \boldsymbol{f}_i^{ext} + \sum_{j,j\neq i} (f_n^{ij}\boldsymbol{n}_{ij} + \boldsymbol{f}_t^{ij}) \quad \forall i = 1 \dots N,$$
$$J_i \dot{\boldsymbol{\omega}}_i = \sum_{j,j\neq i} (\boldsymbol{r}_i \wedge \boldsymbol{f}_t^{ij}) \quad \forall i = 1 \dots N.$$

This corresponds to Newton's second law, for which the contact between two particles i and j induces the force $f_n^{ij}\boldsymbol{n}_{ij} + \boldsymbol{f}_t^{ij}$ on particle i. From the definition of f_n^{ji} and $\boldsymbol{f}_t^{ji}$ from f_n^{ij} and $\boldsymbol{f}_t^{ij}$ the action of this contact is reciprocal on both particles. The normal force exerted on sphere i due to this contact is $f_n^{ij}\boldsymbol{n}_{ij}$ and $\boldsymbol{f}_t^{ij} \in \Pi_{ij}$ is the frictional (tangential) force, which belongs to the plane orthogonal to $\boldsymbol{n}_{ij}$.

From Equation (2) we have $f_n^{ij} = f_n^{\alpha} \geq 0$. This, together with the orientation of $\boldsymbol{n}_{ij}$ from particle j to particle i ensures that this force is repulsive, as expected. Equation (2) also ensures that the distances between the particles remains positive and that the normal force is null whenever the distance is strictly positive (i.e., the particles are not in contact).

Finally, Equations (3) and (4) reflect the classical Coulomb law for friction, linking the normal and tangential contact forces.

2.1. Time-stepping scheme

In the spirit of Refs. [51,52], we follow a strategy based on a semi-implicit discretization for problem (1)-(4), together with a convexification of the non-overlapping constraint. It is a first order scheme with a time step denoted $\Delta t : t^{k+1} = t^k + \Delta t$. Considering a configuration $\boldsymbol{c}^k$ at time $k\Delta t$, we define the set I_c and the operators P_α, A_α as previously. They all depend on the current configuration $\boldsymbol{c}^k$, but we shall drop this explicit dependence to alleviate notation.

Denoting by $\boldsymbol{u}^k \in \mathbb{R}^{6N}$ the generalized velocity at step k, the discrete problem writes: find $\boldsymbol{u}^{k+1} \in \mathbb{R}^{6N}$, $f_n^\alpha \in \mathbb{R}$ and $\boldsymbol{f}_t^\alpha \in \mathbb{R}^3$ for $\alpha \in I_c$ such that

$$\mathrm{M}\,\frac{\boldsymbol{u}^{k+1} - \boldsymbol{u}^k}{\Delta t} = \mathbf{f}^{ext} + \sum_{\alpha \in I_c} A_\alpha^T \left(f_n^\alpha \boldsymbol{n}_\alpha^k + \boldsymbol{f}_t^\alpha \right), \tag{5}$$

$$f_n^\alpha \geq 0, \; D_\alpha(\boldsymbol{c}^k) + \Delta t \nabla D_\alpha(\boldsymbol{c}^k) \cdot \boldsymbol{u}^{k+1} - \Delta t\, \mu \left| P_\alpha^k A_\alpha \boldsymbol{u}^{k+1} \right| \geq 0, \quad \alpha \in I_c,$$
$$f_n^\alpha \left(D_\alpha(\boldsymbol{c}^k) + \Delta t \nabla D_\alpha(\boldsymbol{c}^k) \cdot \boldsymbol{u}^{k+1} - \Delta t\, \mu \left| P_\alpha^k A_\alpha \boldsymbol{u}^{k+1} \right| \right) = 0 \quad \alpha \in I_c, \tag{6}$$

$$\text{If } P_\alpha^k A_\alpha \boldsymbol{u}^{k+1} \neq 0 \text{ (sliding motion)}, \; \boldsymbol{f}_t^\alpha = -\mu f_n^\alpha \frac{P_\alpha^k A_\alpha \boldsymbol{u}^{k+1}}{\left| P_\alpha^k A_\alpha \boldsymbol{u}^{k+1} \right|} \quad \alpha \in I_c, \tag{7}$$

$$\text{If } P_\alpha^k A_\alpha \boldsymbol{u}^{k+1} = 0 \text{ (no slip)}, \; \left| \boldsymbol{f}_t^\alpha \right| \leq \mu f_n^\alpha \quad \alpha \in I_c. \tag{8}$$

Equation (5) is an Euler discretization of Newton's law (1). Equations (7) and (8) are the implicit discretization of Coulomb law (3), (4). Concerning (6), the convexified discrete constraint writes

$$D_\alpha(\boldsymbol{c}^k) + \Delta t \nabla D_\alpha(\boldsymbol{c}^k) \cdot \boldsymbol{u}^{k+1} \geq \Delta t\, \mu \left| P_\alpha^k A_{ij} \boldsymbol{u}^{k+1} \right|. \tag{9}$$

If $\boldsymbol{c}^{k+1} = \boldsymbol{c}^k + \Delta t\, \boldsymbol{v}^{k+1}$, using a Taylor expansion, one has

$$D_\alpha(\boldsymbol{c}^{k+1}) \geq \Delta t\, \mu \left| P_\alpha^k A_{ij} \boldsymbol{u}^{k+1} \right| + O(\Delta t^2),$$

which can be seen as a first order implicit approximation of (2). Note that, due to the convexity of the distance function, this constraint returns feasible configurations. More precisely,

$$D_\alpha(\boldsymbol{c}^{k+1}) \geq D_\alpha(\boldsymbol{c}^k) + \Delta t \nabla D_\alpha(\boldsymbol{c}^k) \cdot \boldsymbol{u}^{k+1} \geq \Delta t\, \mu \left| P_\alpha^k A_{ij} \boldsymbol{u}^{k+1} \right| \geq 0,$$

which may be strictly positive, especially when the tangential velocity is high.

2.2. Numerical resolution

A straightforward discretization of the non-overlapping constraint $D_\alpha(\boldsymbol{c}^k) + \Delta t \nabla D_\alpha(\boldsymbol{c}^k) \cdot \boldsymbol{u}^{k+1} \geq 0$ would have led to a Linear Complementarity Problem. This strategy has been chosen in Refs. [37–43]. Convexifying the constraint, the discretized problem

(5)-(8) now takes the form of a Cone Complementarity Problem (CCP). Some authors have proposed an approach based on this formulation, using Projected Jacobi and Gauss-Seidel Jacobi methods [52–55]. These methods have a linear convergence rate, and require several iterations on the potential contacts. The computational cost of these methods are known to become prohibitive for a large number of particles and contacts.

More efficient strategies can be used, taking advantage of the fact that, as stated in Refs. [51,52], the time-stepping scheme (5)-(8) can be identified to the set of Euler conditions associated to a conic constrained optimization problem, based on the global force vector as unknown. For example, one can use Accelerated Projected Gradient Descent [59,80] or various Krylov subspace and spectral methods [58] to solve the corresponding optimization problem. These algorithms still have a linear convergence rate, but they provide significant reductions in the number of iterations. Finally, to further reduce the number of iterations of the solvers, one can use numerical methods with quadratic convergence rate. For example, the classical Primal-Dual Interior-Point was used in Refs. [56,81,57] to solve the conic optimization problem corresponding to (5)-(8). As expected, due to the quadratic rate of convergence, the number of iterations required to achieve a given accuracy is greatly reduced compared to first order methods. However, these methods require a Newton step to compute the descent direction and can lose their competitive advantage compared to first order methods for large number of particles. See, e.g., Ref. [60] for a comparison of the efficiency of first and second order methods to solve Problem (5)-(8). Improving the available algorithms to solve problem (5)-(8) is still an active domain of research. One can cite for example the recent works [61,80] where the authors propose a method to accelerate the Newton step in second-order methods.

This convexified approach (5)-(8) is very promising, especially under its optimization-based formulation. Indeed, compared to soft methods like MD, the implicit treatment of the constraint allows to use large time steps. Moreover, compared to non-convex hard methods, each time step relies on the resolution of a single conic constrained optimization problem. Therefore, we can take advantage of the many existing solvers for this type of problem and of any improvement that would be made to them. The good behavior of the convexified discretization has been shown through theoretical results in Ref. [51] and through comparison with experiments, e.g., in Ref. [60].

The previous mentioned methods rely on an optimization problem based on the global force vector as unknown. Following Ref. [62], where the contact problem without friction is tackled, we rephrase it as its dual counterpart: an optimization problem based on the global velocity vector. We prove that this global formulation leads again to the convexified time discretization (5)-(8) and propose in Sec. 3 a parameterization of solver MOSEK [79] to solve this velocity-based formulation.

2.3. A velocity-based variational formulation

We consider in the following the velocity-based constrained minimization problem (referred to as Convex Optimization Contact Dynamics (COCD))

$$\min_{\boldsymbol{u}\in K} J(\boldsymbol{u}) \tag{10}$$

$$J(\boldsymbol{u}) = \frac{1}{2}\boldsymbol{u}\cdot M\boldsymbol{u} - \boldsymbol{u}\cdot M\boldsymbol{U}^{k+1}\,,\ \boldsymbol{U}^{k+1} = \boldsymbol{u}^k + \Delta t\, M^{-1}\mathbf{f}^{ext}\,,$$

$$K = \left\{\boldsymbol{u}\,,\ g_\alpha(\boldsymbol{u}) \le 0, \alpha \in I_c\right\}\,,\ g_\alpha(\boldsymbol{u}) = -D_\alpha(\boldsymbol{c}^k) - \Delta t\,\nabla D_\alpha(\boldsymbol{c}^k)\cdot\boldsymbol{u} + \mu\Delta t\left|P_\alpha^k A_\alpha \boldsymbol{u}\right|.$$

As stated in Refs. [51,52] for the force-based optimization problem, the local contact properties can be recovered from (10) by noticing that the discretized scheme (5-8) corresponds the optimality conditions of this global velocity-based optimization problem. In the following, we derive rigorously these optimality conditions for the velocity-based problem and prove that if $\boldsymbol{u}^{k+1}$ is the solution to this convex minimization problem then, it is solution to (5)-(8), for some set of forces $(f_n^\alpha \boldsymbol{n}_{ij} + \boldsymbol{f}_t^\alpha)_{\alpha\in I_c}$ to be determined. To write the Euler equations of this constrained problem, note that the constraints g_α are not differentiable at point $\boldsymbol{u}$ where $P_\alpha^k A_\alpha \boldsymbol{u} = 0$. As a consequence, if the solution verifies this condition, one will need to use the sub-differential of g_α at this point instead of its classical derivatives to write Euler equations.

By definition, for $h : \mathbb{R}^3 \to \mathbb{R}$, the sub-differential $\partial h[\boldsymbol{u}]$ of a function h at point $\boldsymbol{u}$ is the set of directions $\boldsymbol{v}$ for which the line, issued from $h(\boldsymbol{u})$ and following direction $\boldsymbol{v}$ remains below the graph of h:

$$\partial h[\boldsymbol{u}] = \left\{\boldsymbol{v}\in\mathbb{R}^3 \ /\ \forall \hat{\boldsymbol{u}}\in\mathbb{R}^3\,,\ h(\hat{\boldsymbol{u}}) \ge h(\boldsymbol{u}) + \boldsymbol{v}\cdot(\hat{\boldsymbol{u}} - \boldsymbol{u})\right\}$$

It is easy to show from this definition that, if h is differentiable at point $\boldsymbol{u}$ then the set is a singleton: $\partial h[\boldsymbol{u}] = \{\nabla h(\boldsymbol{u})\}$. In case of non-differentiable constraints, the optimization problem (10) fits into the framework detailed in Ref. [82, Th. 2.1.4 p. 305]. Under the condition that the constraints are *qualified* (see below), there exist Lagrange multipliers $(\gamma_\alpha)_{\alpha\in I_c}$ such that

$$\nabla_u J(\boldsymbol{u}) \in -\sum_{\alpha\in I_c} \gamma_\alpha\, \partial g_\alpha[\boldsymbol{u}] \tag{11}$$

$$\gamma_\alpha \ge 0\,,\ \gamma_\alpha g_\alpha(\boldsymbol{u}) = 0 \quad \alpha\in I_c \tag{12}$$

Note that, when the constraints are differentiable, we recognize here the classical Euler equations for the minimization problem.

The aforementioned qualification of the constraint can be checked easily in the present situation. It amounts to show that the interior of the feasible set is non-empty (Slater condition), which is the case here. Indeed, the velocity vector

$$\boldsymbol{u}_0 = (\epsilon \boldsymbol{c}_1, 0, \dots, \epsilon \boldsymbol{c}_N, 0),$$

with $\epsilon > 0$, lies in the interior of K.

It now remains to compute the sets $\partial g_\alpha[\boldsymbol{u}]$ for any $\boldsymbol{u}$. To do so, let us first decompose g_α in two terms:

$$g_\alpha = g_\alpha^n + g_\alpha^t, \; g_\alpha^n(\boldsymbol{u}) = -D_\alpha(\boldsymbol{c}^k) - \Delta t \nabla D_\alpha(\boldsymbol{c}^k)\cdot \boldsymbol{u}, \; g_\alpha^t(\boldsymbol{u}) = \mu \Delta t \left| {P_\alpha}^k A_\alpha \boldsymbol{u} \right|$$

Since g_α^n is differentiable, it is easy to see that

$$\partial g_\alpha^n[\boldsymbol{u}] = \left\{ -\Delta t \nabla D(\boldsymbol{c}^k) \right\} = \left\{ -\Delta t \, A_\alpha^T \boldsymbol{n}_\alpha^k \right\}$$

To compute $\partial g_\alpha^t[\boldsymbol{u}]$, we use the following result: if $P : \mathbb{R}^3 \to \mathbb{R}^3$ is the projection on a given plane Π and h is defined as $h(u) = |P\boldsymbol{u}|$

$$\text{If } P\boldsymbol{u} \neq 0, \; \partial h[\boldsymbol{u}] = \left\{ \frac{P\boldsymbol{u}}{|P\boldsymbol{u}|} \right\}$$

$$\text{If } P\boldsymbol{u} = 0, \; \partial h[\boldsymbol{u}] = \left\{ \boldsymbol{v} \in \mathbb{R}^3 \; / \; \boldsymbol{v} \in \Pi \text{ and } |\boldsymbol{v}| \leq 1 \right\}$$

From this we obtain [82, Th. 4.2.1 p. 263]

$$\text{If } P_\alpha^k A_\alpha \boldsymbol{u} \neq 0, \; \partial g_\alpha^t[\boldsymbol{u}] = \left\{ \mu \Delta t \, A_\alpha^T \frac{P_\alpha^k A_\alpha \boldsymbol{u}}{\left| P_\alpha^k A_\alpha \boldsymbol{u} \right|} \right\}$$

$$\text{If } P_\alpha^k A_\alpha \boldsymbol{u} = 0, \; \partial g_\alpha^t[\boldsymbol{u}] = \left\{ \mu \Delta t \, A_\alpha^T \boldsymbol{v} \; / \; \boldsymbol{v} \in \Pi_\alpha^k \text{ and } |\boldsymbol{v}| \leq 1 \right\}$$

where we recall that Π_α^k is parallel to the tangent plane, perpendicular to $\boldsymbol{n}_\alpha^k$. We finally obtain the sub-differential of g_α:

$$\text{If } P_\alpha^k A_\alpha \boldsymbol{u} \neq 0, \; \partial g_\alpha[\boldsymbol{u}] = \left\{ \Delta t \, A_\alpha^T \left(-\boldsymbol{n}_\alpha^k + \mu \frac{P_\alpha^k A_\alpha \boldsymbol{u}}{\left| P_\alpha^k A_\alpha \boldsymbol{u} \right|} \right) \right\}$$

$$\text{If } P_\alpha^k A_\alpha \boldsymbol{u} = 0, \; \partial g_\alpha[\boldsymbol{u}] = \left\{ \Delta t \, A_\alpha^T \left(-\boldsymbol{n}_\alpha^k + \mu \boldsymbol{v} \right) \; / \; \boldsymbol{v} \in \Pi_\alpha^k \text{ and } |\boldsymbol{v}| \leq 1 \right\}$$

So from (11), (12), we obtain that, if $\boldsymbol{u}^{k+1}$ is solution to (10) there exists Lagrange multipliers $(\gamma_\alpha)_{\alpha \in I_c}$ such that

$$M\boldsymbol{u}^{k+1} - M\boldsymbol{U}^{k+1} = -\Delta t \sum_{\alpha \in I_c} A_\alpha^T \left(-\gamma_\alpha \boldsymbol{n}_\alpha^k + \mu \gamma_\alpha \boldsymbol{v} \right)$$

$$\gamma_\alpha \geq 0, \; \gamma_\alpha g_\alpha(\boldsymbol{u}) = 0 \quad \alpha \in I_c$$

$$\text{If } P_\alpha^k A_\alpha \boldsymbol{u}^{k+1} \neq 0 \text{ (sliding motion)}, \; \boldsymbol{v} = \frac{P_\alpha^k A_\alpha \boldsymbol{u}^{k+1}}{\left| P_\alpha^k A_\alpha \boldsymbol{u}^{k+1} \right|} \quad \alpha \in I_c$$

$$\text{If } P_\alpha^k A_\alpha \boldsymbol{u}^{k+1} = 0 \text{ (no slip)} \; , \; \boldsymbol{v} \in \Pi_\alpha^k \text{ and } |\boldsymbol{v}| \leq 1 \quad \alpha \in I_c$$

Using the definition of U^{k+1} and setting $f_\alpha^n = \gamma_\alpha$ and $\boldsymbol{f}_\alpha^t = -\mu \gamma_\alpha \boldsymbol{v}$, we finally obtain that $\boldsymbol{u}^{k+1}$ is solution to the discrete problem (5)-(8), as expected.

3. Computational aspects

In the current section, we present a conic version of the minimization problem (10) that can be adapted in solver MOSEK [79]. First, we describe the conic formulation in MOSEK, introduce the Primal-Dual Interior-Point algorithm, define the solver termination criteria and reduce the number of variables and constraints. We discuss the numerical parameters values: the time step and the solver tolerance in a second time. Finally, we validate the COCD with another "hard" method, the Non-Smooth Contact Dynamics (NSCD) method. The complete set of parameters for each simulation are given in Appendix in Table A.2.

3.1. Implementation in convex solver MOSEK

According to MOSEK's documentation, solving a conic version of the Quadratic Program (10) is preferable for computational efficiency. This Quadratic Program is then reformulated into a Conic Optimization Program as follows. First, the quadratic term in the objective functional J in (10) is replaced by t, together with a new conic constraint $\boldsymbol{u} \cdot M\boldsymbol{u} \leq 2t$. Then, the constraints $g_\alpha(\boldsymbol{u}) \leq 0$ in (10) is also rewritten as a simple conic constraints $\left| x'_\alpha \right| \leq y'_\alpha$. To do so, we introduce the new variables x'_α and y'_α, together with the new linear equality constraints $x'_\alpha = \mu \Delta t \, P_\alpha^k A_\alpha \boldsymbol{u}$ and $y'_\alpha = D_\alpha(\boldsymbol{c}^k) + \Delta t \nabla D_\alpha(\boldsymbol{c}^k)\cdot \boldsymbol{u}$. This leads to the new equivalent minimization problem

$$\min_{t, \boldsymbol{u}, x', y'} t + \boldsymbol{u} \cdot M\boldsymbol{U}^{k+1}, \tag{13}$$

under the constraints

$$x'_\alpha = \mu \Delta t\, P^k_\alpha A_\alpha \boldsymbol{u}\,,\ y'_\alpha = D_\alpha(\boldsymbol{c}^k) + \Delta t\, \nabla D_\alpha(\boldsymbol{c}^k)\cdot \boldsymbol{u}\,,\ \alpha \in I_c\,,$$
$$\left|x'_\alpha\right| \le y'_\alpha\,,\ \alpha \in I_c \quad \text{and} \quad \boldsymbol{u}\cdot M\boldsymbol{u} \le 2t\,,\ .$$

Finally, setting $x = (t, \boldsymbol{u}, x', y')$, problem (13) can be written under the form of a Conic Optimization Program:

$$\min_x\ c\cdot x, \quad \text{subject to} \quad Ax = b, \quad \text{and} \quad x \in \mathcal{K}, \tag{14}$$

where $\mathcal{K}$ is a convex cone which is the cross product of all the conic constraints in (13). The corresponding dual problem of (14) is

$$\max_y\ b\cdot y, \quad \text{subject to} \quad A^{\mathrm{t}} y + s = c, \quad \text{and} \quad s \in \mathcal{K}^\star, \tag{15}$$

where $\mathcal{K}^\star$ is the dual cone of $\mathcal{K}$.

3.2. Definition of MOSEK's termination criteria

MOSEK computes a solution with a Primal-Dual Interior Point Algorithm. It consists in solving the following homogeneous problem:

$$\begin{array}{rcll} A\tilde{x} - b\tilde{\tau} & = & 0, & \tilde{x} \in \mathcal{K}, \\ A^{\mathrm{t}}\,\tilde{y} + \tilde{s} - c\tilde{\tau} & = & 0, & \tilde{s} \in \mathcal{K}^\star, \\ -c^{\mathrm{t}}\,\tilde{x} + b^{\mathrm{t}}\,\tilde{y} - \tilde{\kappa} & = & 0, & \tilde{\tau},\, \tilde{\kappa} \ge 0, \end{array} \tag{16}$$

where $\tilde{\tau}$ and $\tilde{\kappa}$ are two additional scalar variables and $(x, y, s) = (\tilde{x}/\tilde{\tau},\, \tilde{y}/\tilde{\tau},\, \tilde{s}/\tilde{\tau})$. Problem (16) is a necessary optimality condition for the minimization problem (14). The algorithm generates a sequence of trial solution $\left(x^k, y^k, s^k, \tau^k, \kappa^k\right)$ of (16). If $\varepsilon_p, \varepsilon_d, \varepsilon_g$ are non-negative user specified tolerances, the termination criteria is

$$\max\left(\rho^k_p, \rho^k_d, \rho^k_g\right) \le 1$$

where

$$\rho^k_p = \arg\min_\rho \left\{ \rho \in \mathbb{R} \,/\, \left\| A\frac{x^k}{\tau^k} - b \right\|_\infty \le \rho\varepsilon_p \left(1 + \|\, b\,\|_\infty\right) \right\},$$
$$\rho^k_d = \arg\min_\rho \left\{ \rho \in \mathbb{R} \,/\, \left\| A^{\mathrm{t}}\frac{y^k}{\tau^k} + \frac{s^k}{\tau^k} - c \right\|_\infty \le \rho\varepsilon_d \left(1 + \|\, c\,\|_\infty\right) \right\},$$
$$\rho^k_g = \arg\min_\rho \left\{ \rho \in \mathbb{R} \,/\, \left(\frac{\left((x^k)\right)^{\mathrm{t}} s^k}{(\tau^k)^2}, \left| \frac{(c)^{\mathrm{t}}\, x^k}{\tau^k} - \frac{(b)^{\mathrm{t}}\, y^k}{\tau^k} \right| \right) \le \rho\varepsilon_g \left(1, \frac{\min\left(|(c)^{\mathrm{t}}\, x^k|, |(b)^{\mathrm{t}}\, y^k|\right)}{\tau^k} \right) \right\}.$$

The values we chose for $\varepsilon_p, \varepsilon_d, \varepsilon_g$ are precised in Sec. 3.4.2.

3.3. Number of variables and constraints

In problem (13), all the constraints between grains are considered, and the problem size dramatically increases with the number of particles. However, grains far away from each other may not enter in contact during the current time integration. It is then unnecessary to consider all these potential contacts for every integration step. A simple but efficient way to reduce the number of contacts is to restrict the constraints to pairs of particles for which the distance is less than a prescribed threshold value $\bar{D}$.

Let us define the set $I_c(\bar{D})$ as the subset of I_c of all pairs of particles closer than the prescribed threshold $\bar{D}$:

$$I_c(\bar{D}) = \left\{ \alpha \in I_c \,/\, D_\alpha(\boldsymbol{c}^k) \le \bar{D} \right\}.$$

We then chose to consider, at each time step, the pairs of particles belonging to $I_c(\bar{D})$ rather than I_c.

3.4. Numerical parameters

3.4.1. Time step

To optimize the trade-off between accuracy and computational cost, we investigate here the behavior of the error related to the choice of the time step for 2D column collapses; see Table A.2, row 1 in the appendix for the corresponding numerical parameters. We thus compare the snapshot profiles obtained with different Δt and measure the error with profiles obtained for the smallest value of Δt. Fig. 2(a) represents snapshot profiles at times $t = 0.02\,\mathrm{s}$, $0.06\,\mathrm{s}$ and $0.30\,\mathrm{s}$ for $\Delta t = 10^{-3}\,\mathrm{s}$, $10^{-4}\,\mathrm{s}$ and $5.0\,10^{-5}\,\mathrm{s}$. The relative error between the profiles and those calculated with the reference value of $\Delta t = 5.0\,10^{-5}\,\mathrm{s}$ is shown in Fig. 2(b). The errors are computed as $\mathrm{e}_{\Delta t} = \left\| y_{\Delta t} - y_{ref} \right\| / \left\| y_{ref} \right\|$, where the reference profile is denoted y_{ref} and the other profiles $y_{\Delta t}$.

Fig. 2(a) shows an excellent quantitative agreement between profiles, especially for $\Delta t = 10^{-4}\,\mathrm{s}$ and $5.0\,10^{-5}\,\mathrm{s}$. Even though the value $\Delta t = 10^{-3}\,\mathrm{s}$ is quite large compared to the reference value, the profiles are still very close, with only slight differences. It comforts us that using relatively large time steps with our method does not significantly impact the flow behavior and deposit. Note that, a few time steps are larger than $10^{-3}\,\mathrm{s}$ and this is already very high compared to "soft" methods like MD where largest value

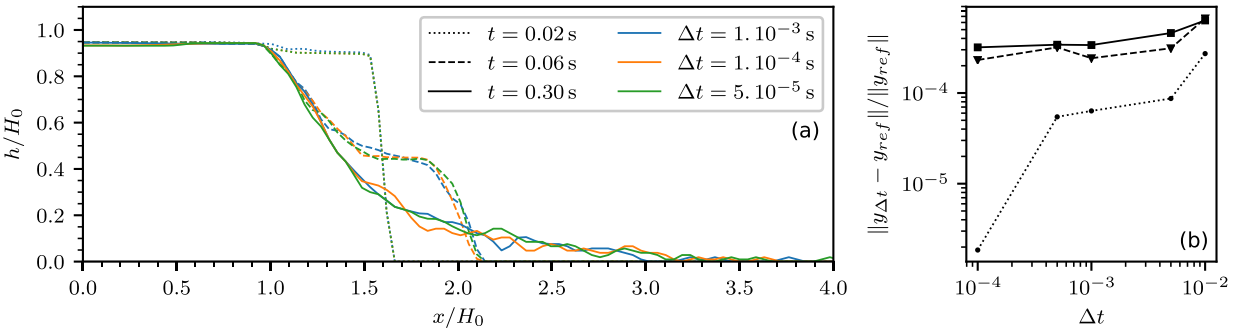

Fig. 2. Influence of the time step variations. These 2D simulations have been carried out with the parameters given in Table A.2, row 1. The plane is horizontal ($\alpha = 0°$), and disks are glued on it. The snapshot profiles are taken at times $t = 0.02\,s$, $0.06\,s$ and $0.30\,s$ for $\Delta t = 10^{-3}\,s$, $10^{-4}\,s$ and $5.0\,10^{-5}\,s$. The time step values have been varied from $\Delta t = 10^{-2}\,s$ to $\Delta t = 5.0\,10^{-5}\,s$. (For interpretation of the colors in the figure(s), the reader is referred to the web version of this article.)

Table 1
Statistics on computational time. The first column gives the simulation name. Then N is the number of disks (2D) or spheres (3D), N_c is the number of potential contacts, Δt is the time step, ϵ is MOSEK's tolerance parameter, Nb(iter.) is the number of iterations required by MOSEK to complete the computation, and time (in seconds) indicates the time needed by MOSEK to complete the problem. N_c, Nb(iter.) and time are computed on ten iterations, from 0.11 s to 0.12 s for *variation of* N and from 1 s to 1.1 s for *variation of* μ. The simulation parameters are given in Table A.2, rows 2 and 4. Any empty cell is equal to the cell value of the row above. The simulations were performed with two Intel Xeon E5-2650 2.00 GHz (2×8 cores) processors on the S-CAPAD platform, IPGP, France.

	name	dimension	N	N_c	Δt (s)	ϵ	Nb (iter.)	time (s)
1	*variation of* N	2D	8 308	37 331	10^{-3}	10^{-8}	47	8.85
2			50 772	238 659			61	51.9
3	*variation of* μ	3D	122 932	829 505	10^{-2}	10^{-8}	21	475.8
4						10^{-5}	11	269.9

are $\Delta t \simeq 10^{-6}\,s$; see Ref. [34]. As expected, Table 1 shows that 3D simulations are more time-consuming than 2D. In the following, we set Δt to $10^{-3}\,s$ for 2D simulations and $10^{-2}\,s$ for 3D. These values are classical in other "hard" methods; see Refs. [83,84].

3.4.2. Tolerance parameter

The default tolerance parameters in MOSEK are set to $\epsilon_p = \epsilon_d = \epsilon_g = \epsilon = 10^{-8}$. Table 1 shows statistics about computational time for 2D and 3D column collapses. These statistics have been generated considering two simulation cases, named *variation of* N (2D) and *variation of* μ (3D); see the values of the parameters in Table A.2, rows 2 and 4. At this stage, we chose these simulations because they are representative of the computational need we have in our study of granular flows on erodible beds in Sec. 5. Indeed, our simulations in Sec. 5 consider grains' mean diameters close to those in experiments (1 mm in our simulations against 0.7 mm in the experiments; see Table A.3). Consequently, the number of grains required in our 2D simulations is $N = 44\,996$, and about 122 000 in our 3D simulations (Table A.3), and these numbers are close to those of simulations *variation of* N (50 000), and *variation of* μ (112 459).

The results presented in Table 1, rows 1 and 2 show that there is no need to tune the default MOSEK's tolerance parameter for 2D simulations since for $\epsilon = 10^{-8}$, one single iteration time is about 51.9 s, which is still reasonable to us. However, Table 1 shows that 3D simulations (rows 3 and 4) requires more than 475 s for a single iteration, which is too large according to us. From the time step values that have been chosen for 3D simulations ($\Delta t = 10^{-2}$ s), it is unnecessary and time-consuming to keep the best MOSEK's default tolerance parameter. To efficiently compute the 3D solutions with COCD, we investigated the influence of the tolerance parameter ε. Considering $\Delta t = 10^{-2}$ s, the choice of ε is made to conserve the stability of a static assembly and is tested for spheres at rest into a box (the box is the initial state of simulation *variation of* μ). As shown in Fig. 3, if ε is larger than 10^{-5}, some instabilities can appear, resulting in non-negligible kinetic energy E_k compared to total energy E_{tot}. Moreover, the mean computational time for a single iteration is about 270 s (see Table 1), which is 43% faster than for $\varepsilon = 10^{-8}$. Consequently, according to these arguments, we chose to get a tolerance parameter about $\varepsilon = 10^{-5}$ for all our 3D simulations because it both maintains a precise computation of assemblies at rest (Fig. 3), while it is sufficiently fast for our study (Table 1).

3.5. Validation: comparison with NSCD

We compared our results with another well-known method (NSCD), extensively studied and compared with laboratory experiments. This method, fully described in Ref. [47], is based on a straightforward time-stepping scheme of the continuous prob-

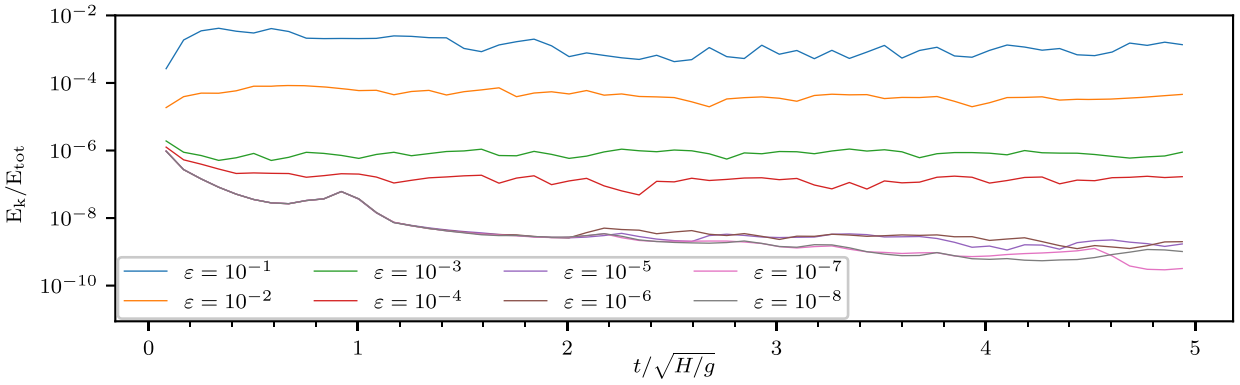

Fig. 3. Kinetic energy rate as a function of the tolerance parameter ε. This 3D test that has been used to study the influence of ε on the stability of a static configuration where a large assembly of rotational spheres ($N = 110\,233$) stays at rest in a rectangular box. This static state is conserved for $\varepsilon \leq 10^{-5}$. The simulation parameters can be found in Table A.2, row 4.

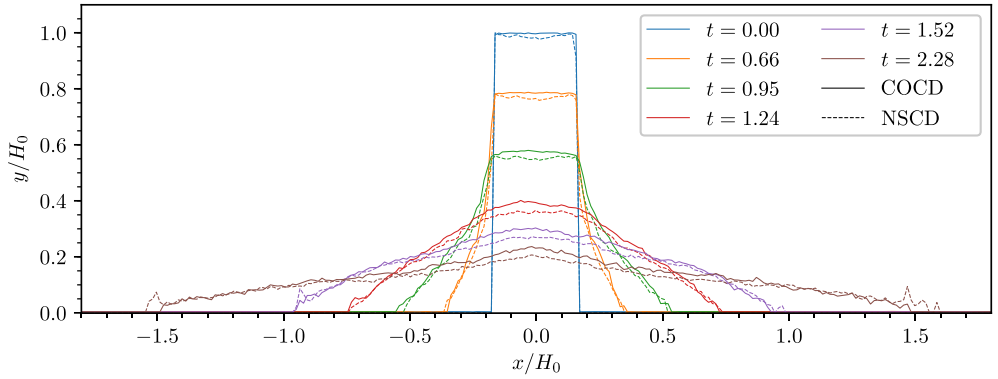

Fig. 4. Comparison of profiles between NSCD and COCD. The reference simulation is a column collapse. In the NSCD simulation [48,49,47,17], there are 6 036 disks and in COCD, $N = 7\,740$; see Table A.2, row 3. The plane is horizontal ($\alpha = 0°$). Note that the times given in the legend are normalized by $\sqrt{H_0/g}$.

lem (1)-(4). The constraint is treated using a first-order approximation, and no convexification is added. The (non-convex) resulting discrete problem is solved using a Gauss-Seidel-like method, iterating on the contacts.

To compare our scheme with this NSCD algorithm, we run a 2D column collapse with the same parameters as in the simulation published in Ref. [48]; both methods parameters are given in Table A.2, row 3. Note that our model is inelastic while the results in Ref. [48] are obtained for an elastic coefficient $e_n = 0.5$. The mass profiles simulated with the two methods are very close as observed in Fig. 4. It shows that considering a purely inelastic model provides sufficient approximation of the flow dynamics, especially in the context of column collapses. Note that the authors of Ref. [48], in the later publication [49], also did not observe significant changes in the final deposits when varying the elasticity coefficient for small values. Consequently, the inelastic assumption will still be considered for applications in the next section, devoted to granular flows on erodible beds.

The good agreement between the simulations with the two methods shows that convexifying the constraint in our numerical algorithm has a very small impact on the macroscopic results for the applications considered in this article.

4. Comparison and calibration with experiments of column collapses on rigid beds

After having set the numerical parameters such as the time step or termination criteria as indicated in Sec. 3, let us calibrate the friction coefficient used in the model by quantitatively comparing the results with laboratory-scale experiments of granular column collapses over inclined rigid beds performed in Refs. [63] and [64] and referred to as *M2010* and *F2014*, respectively. Note that in the COCD model, only one rheological parameter is involved, which is the grain/grain friction coefficient μ that is assumed to be the same as the grain/walls friction coefficient.

4.1. Calibration of the friction coefficient in 3D

The laboratory-scale experiments used here to calibrate the model consist in the release of a granular column of thickness $H_0 = 14$ cm, length $R_0 = 20$ cm (i.e., aspect ratio $H_0/R_0 = 0.7$) on horizontal or inclined channels of different slopes and of width $W = 10$ cm in *M2010* and $W = 20$ cm in *F2014*. In these experiments, the initial mass is released from rest by opening a gate while in our simulations we assume that the mass is released instantaneously. The set-up parameters can be found in Table A.2,

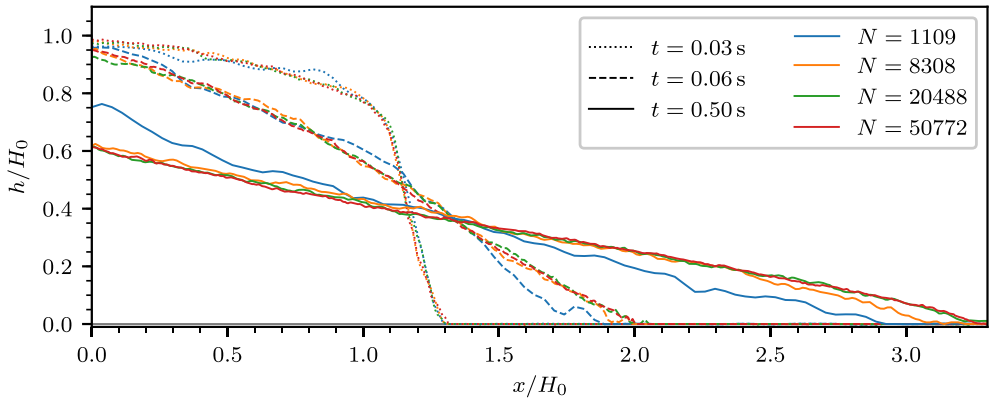

Fig. 5. Comparison of profiles at three different times involving four numbers of grains. For a column collapse on a rigid rough plane, all the simulation parameters are fixed, except for the number of particles $N = 1109$, 8 308, 20 488, and 50 772; see Table A.2, row 2. The plane is horizontal ($\alpha = 0°$).

rows 7 (*M2010*) and 8 (*F2014*) for experiments and row 4 for our simulations. Quantitative comparison of DEM simulations and 3D experiments is difficult since the number of grains is generally too high in the experiments to be accounted for in simulations at a reasonable computational cost.

However, the effects of changing the number of grains have already been studied in Ref. [12] for 3D column collapse simulations realized by Molecular Dynamics (MD). In particular, their Fig. 10 shows that the mass profiles are similar when considering $N \geq 8000$ for $\alpha = 0°$ for an aspect ratio $a = 0.7$ and a volume of $5600\,\mathrm{cm}^3$. In these 3D simulations (with the same box dimensions as in Fig. 10 of Ref. [12]), we use 112 459 grains, which is largely sufficient for the results to be independent of this number. The considered diameter ($d = 4$ mm) is about six times larger than the grains used in both experiments ($d \simeq 0.7$ mm). The initial column is built by a uniform rain in the box and with no friction coefficient ($\mu = 0$). When the mass is released, the friction coefficient is set to its non-zero value.

Figs. 6(a,b) compare the simulated and experimental mass profiles at times $t = 0.18\,\mathrm{s}$ and $t = 1.06\,\mathrm{s}$ (for which the mass is at rest) for flows on a horizontal rigid bed within a channel of width $W = 20$ cm. A series of simulations were performed by varying the friction coefficient μ from 0 to 0.8. Fig. 6(a) shows significant differences between the mass profiles simulated with different friction coefficients and the experimental mass profiles. Whatever the friction coefficient, the simulated mass spreads faster than the experimental mass, partly because the initial removal of the gate is not accounted for in the simulations (see Ref. [18] for detailed analysis of the gate effects). The simulated mass obviously spreads faster as the friction coefficient decreases, with the flow going much further for frictionless simulations. At $t = 1.06\,\mathrm{s}$, the mass is at rest (except for $\mu = 0$ where the mass is still flowing) and the deposits are in good quantitative agreement with experiments for simulations with $0.2 \leq \mu \leq 0.8$. The differences between the experiments of *M2010* and *F2014*, mainly due to the different channel widths, are smaller than the differences between the simulated and experimental results whatever the value of μ. However, there is a relatively good agreement between the mass deposit simulated with $\mu = 0.3$ and the two experiments.

Fig. 6(c) represents the time evolution of the relative volume variation $a_v = (V(t) - V_0)/V_0$, where $V(t)$ is the volume occupied by the flow at time t and V_0 is the initial volume. Fig. 6(c) shows that the dilatation increases with increasing μ. This is in good agreement with the CD simulations of Ref. [85] who showed that the dilatation angle increases almost linearly with the grain/grain friction coefficient. However, this increase is far greater than in the experimental measurements [19] (compare the black and colored curves in Fig. 6(c)). Indeed, in experiments, the relative volume variation stays in the range $a_v \in [-2,\ 2]\,\%$, while it goes up to 10% for the simulation with $\mu = 0.2$. Two reasons may explain these differences: The first reason is that the initial mass in the column is built with a null coefficient of friction, as it is usually done in DEM [48,49], allowing the spheres to organize themselves in a higher compacted configuration than for simulations with $\mu \neq 0$. When the gate is removed, the friction coefficient is set to its positive value, explaining a higher initial dilatation corresponding to bead arrangements obtained in the presence of friction. For $\mu = 0$, Fig. 6(c) shows that the volume is more compacted ($a_v \simeq -5\%$). The second reason for initial dilatation can also be the fact that COCD is a Convexified Method (see Introduction) since the normal constraint (9) that is implemented is a convexification of the constraint (6). Consequently, when $\mu \neq 0$, a gap between particles in contact may arise, as a numerical artifact of the relaxation process [57]. However, this numerical artifact seems negligible when comparing with a non-convexified method such as NSCD (see Sec. 3.5).

For our simulations, the best-fit interparticle friction coefficient is $\mu = 0.3$, calibrated by comparing our simulations with experiments *M2010* and *F2014* at $t = 1,06$ s, that is, when the granular mass has stopped. Indeed, it is better to calibrate the friction coefficient on the final deposit that has been shown to be poorly affected by the gate opening [18]. This value is relatively close to the friction coefficients measured for a perfect glass/glass contact ($\mu = 0.4$ [86]) and to those calibrated with Molecular Dynamics methods ($\mu = 0.16$ [87]).

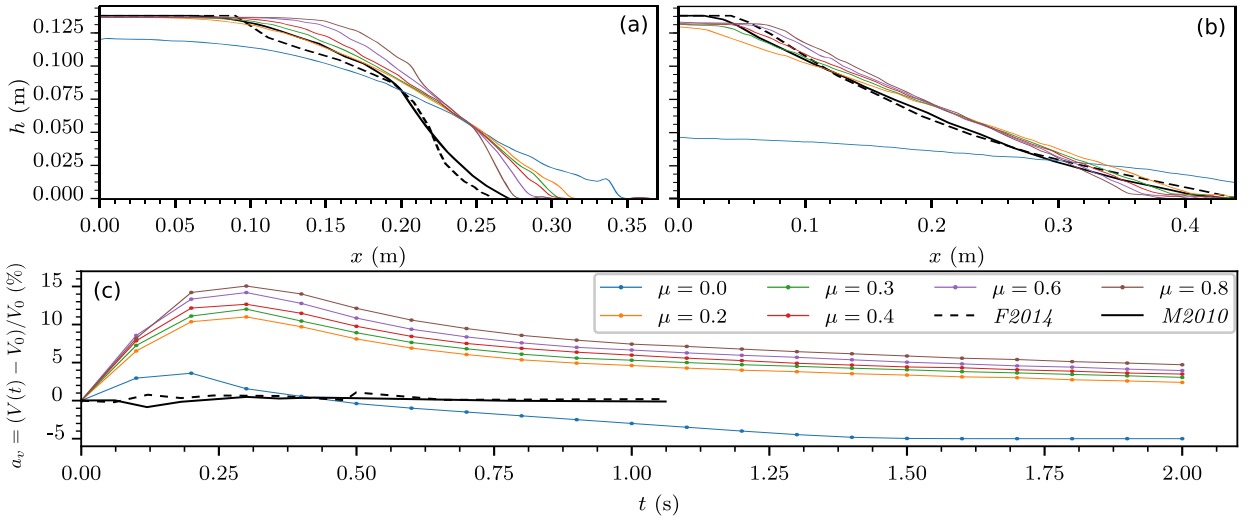

Fig. 6. Comparison between simulations with different values for the friction coefficient. Fig. a (respectively, b) represents mass profiles on a horizontal plane ($\alpha = 0°$) at times $t = 0.18$ s (respectively, 1.06 s). Fig. c represents the relative volume variation $a_v = (V(t) - V_0)/V_0$. These 3D simulations have been performed with the parameters given in Table A.2, row 4 and the characteristics of experiments are given in rows *M2010* and *F2014* of the same table. The experimental results *M2010* ([63]) and *F2014* ([64]) are obtained respectively with $W = 10$ cm and $W = 20$ cm, while $W = 20$ cm in our simulations. The rough plane is horizontal and covered with a layer of glued particles.

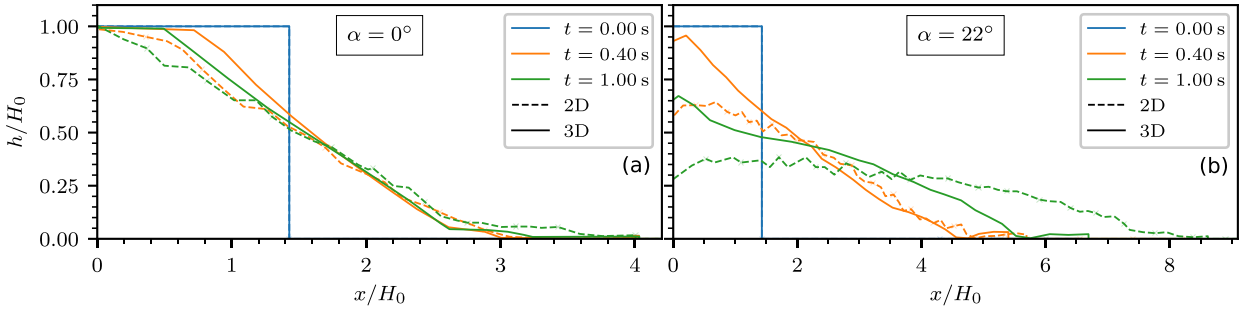

Fig. 7. Comparison of simulated 2D and 3D profiles for two slopes. Fig. a represents the mass profiles at time 0, 0.4, and 1 s for a horizontal plane ($\alpha = 0°$) while Fig. b is for an inclined plane of $\alpha = 22°$. The 2D simulations are represented by dashed curves while 3D simulation are continuous curves. Simulation parameters can be found in Table A.2, rows 5 and 6.

4.2. Calibration of the friction coefficient in 2D

We compare here 2D and 3D simulations computed with the same grain parameters; see Table A.2, rows 5 and 6. For a granular column with the same thickness H_0 and length R_0, we considered $N = 2\,154$ disks in 2D and $N = 112\,459$ spheres in 3D for a channel width $W = 20$ cm (see Fig. 8). Indeed, in 3D the granular mass flows within a channel bounded by two lateral walls, as in the laboratory experiments. Figs. 7(a) and 7(b) represent the mass profiles calculated with 2D and 3D simulations for granular collapse on a horizontal and on a 22° sloping plane, respectively, at different times. The 3D simulation dissipates more kinetic energy than the 2D simulation, especially for high slope angles as already observed in Ref. [88]. For example, at $t = 1.00$ s, the front position is about 12% longer for 2D than for 3D with $\alpha = 0°$ and about 32% longer with $\alpha = 22°$.

The additional degree of freedom for particle motion in 3D may partly explain these differences. In 3D systems, the forward particle motion can be associated with lateral motion, which is not the case in 2D. Frictional dissipation also occurs during lateral particle motion, thus reducing the final distance reached by the grains. Furthermore, particles are in contact with other particles at their lateral sides. Because of wall effects, the velocity of the flowing particles at the center is slightly higher than the velocity of these adjacent particles, thus inducing friction. To correct artificially for missing frictional effects in simulations, the simplest way is to empirically increase the friction coefficient to reproduce laboratory experiments. This fitting procedure has been used, for instance, in 2D continuum simulations in Ref. [19], where they used a higher friction coefficient in the $\mu(I)$-rheology to mimic wall effects, or in 2D COCD simulations in Ref. [88], where they increased interparticle friction to reproduce laboratory-scale experiments (see their Sec. V.D). Following the same strategy, we artificially increase the interparticle friction coefficient up to $\mu = 0.9$ in our 2D simulations to reproduce the experimental runout distance of granular collapse on a horizontal plane, as Ref. [88], leading to a higher fitted friction coefficient than in 3D, where $\mu = 0.3$.

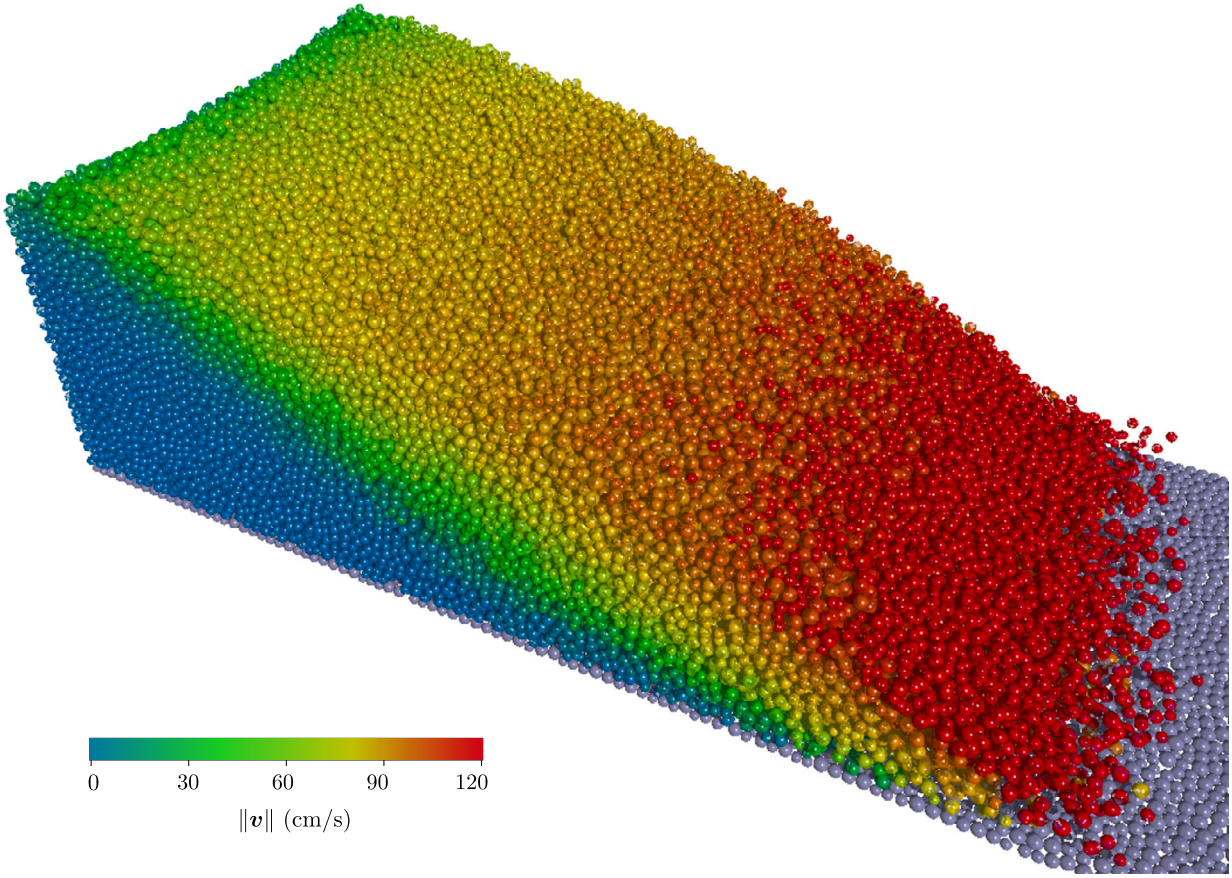

Fig. 8. Snapshot of 3D simulation. This picture is a snapshot at $t = 0.15$ s of the 3D simulation given in Table A.2, row 6 on a horizontal plane ($\alpha = 0°$). The granular assembly is composed of spheres (with 10% of polydispersity) and the flow is confined by two invisible lateral walls and another wall located at the left of the domain. Concerning the bottom, the rough bed is composed of glued spheres with the same grain properties and polydispersity. In this picture, the colors represent the normalized velocity of translation.

Note that in 2D, the effects of the number of grains in such set-ups has been briefly investigated (see Fig. 5) and seems to weakly affect the profiles when $N \geq 20\,000$. For the initial 2D box dimension $R_0 \times H_0 = 20 \times 14\,\text{cm}^2$ that is considered for our study about erodible beds (Sec. 5), this corresponds to the number of grains of mean diameter $d = 1$ mm, which is close to the particle size in the experiments. However, in Fig. 7 we only consider 2 154 grains in our 2D simulations because we want to have the same grain size than in our 3D simulations. The effect of considering a smaller grain size (or equivalently, a larger number of grains in the same initial volume) is to have a longer runout distance until the difference almost vanishes (compare blue, orange, and green curves in Fig. 5). Consequently, the front position in 2D simulations is underestimated in Fig. 7, while it is already much longer than 3D simulations.

5. Granular column collapses on erodible beds

We now highlight the potential of COCD to gain physical insight into the complex dynamics of granular flows on inclined shallow erodible beds with thicknesses of a few to about ten particles. Laboratory experiments have shown that the runout distance of granular flows increases with increasing thickness of the erodible layer up to a critical thickness [63,64]. The interactions between the flowing mass and the erodible bed is expected to depend on grain scale processes through the complex rearrangement of the contact network and momentum exchanges. To reproduce these experiments with discrete simulations, at least qualitatively, the number of grains in the simulation and in the experiments should be roughly similar. This is why the grain size in the simulations should be as close as possible to the real grain size.

However, with a mean particle diameter of $d \simeq 0.7$ mm, the experiments from Ref. [64] (see Table A.3, row 10) involve approximately 20 million grains for an initial column volume $V = 5600\,\text{cm}^3$ and a standard volume fraction $\Phi = 0.64$. Considering the same volume in 3D simulations would thus lead to prohibitive computational times. Therefore, we first perform 2D simulations (Sec. 5.1). We simulate a column with an aspect ratio $a = 0.7$ ($R_0 \times H_0 = 20 \times 14\,\text{cm}^2$) with grains of mean diameter $d = 1$ mm, similar to that of the experiments. Then, with the same mean grain diameter, we compute 3D simulations but reduce the mass volume ($R_0 \times H_0 \times W = 10 \times 7 \times 0.8\,\text{cm}^3$) while keeping the same aspect ratio (Sec. 5.2). As a result, for 2D (Table A.3, rows 1 to 5) and

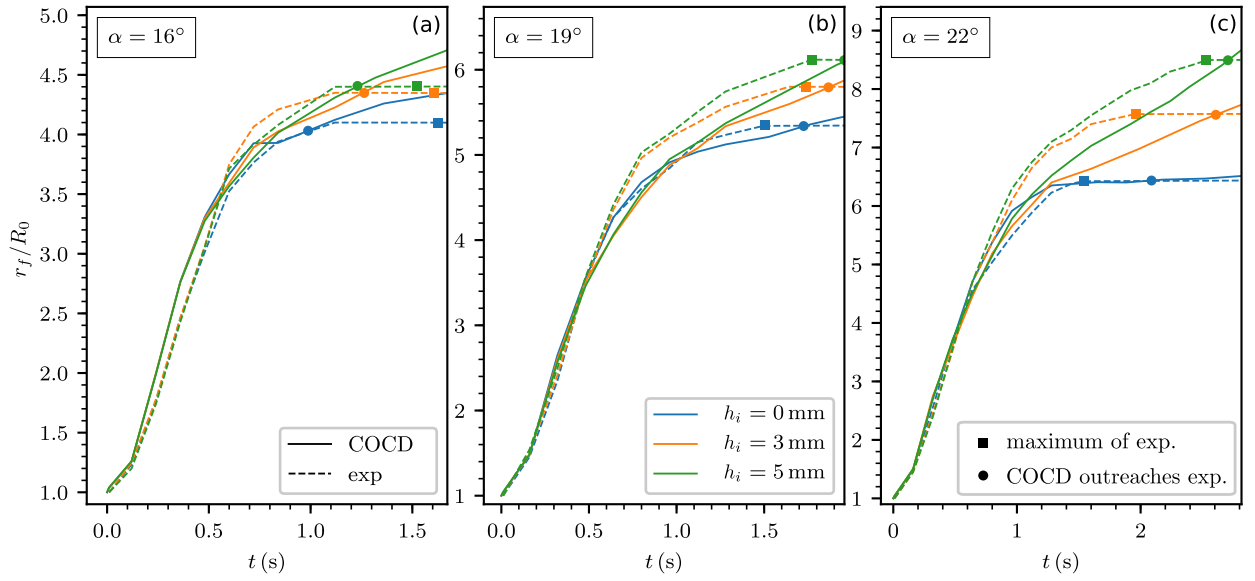

Fig. 9. Evolution of the front position of 2D simulations and experiments. Three inclinations $\alpha = 16, 19$, and $22°$ and three widths of the erodible layer $h_i = 0, 3$, and 5 mm are represented. The grain properties are the same in the column and in the erodible layer. In Table A.3, the simulations correspond to rows 1 to 5 and the experiments to row 10. The experiments were carried out by Farin *et al.* (2014) [64]. Note that the vertical scales differ in Figs. a, b, and c. The squares correspond to the times at which the runout distance is reached in experiments while the circles correspond to the times at which the simulations outdistance the experiments. Note that the final times of simulations are not represented in the figures and that the simulations continue to flow for more than 6 s (see Fig. 11).

3D (Table A.3, rows 7 to 9) simulations, the mean grain size is $d = 1$ mm, while in the 2D simulation highlighting erosion waves (Table A.3, row 6), the grain size is slightly larger ($d = 1.8$ mm).

5.1. 2D simulations: evolution of the mass, velocity profiles and wave motion

5.1.1. Evolution of the granular mass

Fig. 9 represents the evolution of the normalized front position r_f/R_0 of the granular mass. The simulations reproduce quite well the experiments from Ref. [64] up to about $t = 0.6$ s (compare continuous and dashed curves for each color in Figs. 9(a)-(c)). Except for $\alpha = 16°$ (Fig. 9(a)), where the simulations go slightly faster than the experiments, the other simulations at 19° and 22° (Fig. 9(b) and 9(c)) are systematically slower until the time at which the experimental mass front stops (represented by squares in Fig. 9). Subsequently, for $\alpha > 16°$, the simulated front overcomes the experimental front already at rest (this time is represented by circles in Fig. 9).

Similarly to experiments, our simulations show that the thicker the erodible layer, the greater the distance traveled by the flow (compare the blue $h_i = 0$ mm, orange $h_i = 3$ mm, and green $h_i = 5$ mm curves in Fig. 9). This behavior is amplified when the slope increases, as observed experimentally. For example, the maximal difference between $h_i = 3$ and 5 mm is about 10% of R_0 at $\alpha = 16°$ (Fig. 9(a)), 30% at 19° (Fig. 9(b)), and 110% at 22° (Fig. 9(c)). Note that these differences are approximately the same as in the experiments with a larger difference in the traveled distance between $h_i = 0$ mm and $h_i = 3$ mm than between $h_i = 3$ mm and $h_i = 5$ mm.

The main difference between simulations and experiments is that while the experimental granular masses stop (square dots in Fig. 9), the simulated masses continue to spread and therefore ultimately outdistance the experiments (circle dots). This is illustrated in Fig. 10 for granular collapse at $\alpha = 22°$ on an erodible bed of thickness $h_i = 5$ mm. At $t = 0.18$ s (Fig. 10(a)), the simulation goes slightly faster than the experiments, probably related to the initial removal of the gate that is not accounted for in the simulation (see the influence of the gate in Ref. [18]). The experimental and simulated fronts become close at $t \simeq 0.48$ s (Fig. 10(b)). Until this time, the mass profiles are similar. Then, the simulation remains slightly behind but reaches the experiment at $t = 2.7$ s (Figs. 9(c) and 10(c)) while the experiment has stopped at $t = 2.5$ s (Fig. 9(c)). Finally, the simulation continues to flow while the experiment stays at rest (insert 4 in Fig. 10(d)). At $t = 4$ s, the simulated mass has left the left wall (insert 3 in Fig. 10(d)).

As discussed previously, this non-stopping behavior for flows beyond an inclination angle higher than 16° is attributed to 2D simulations. Similar findings were reported by Ref. [88]. Indeed, in 2D simulations, the avalanche angle is approximately 16°, whereas it is around 22° in experiments involving grains with similar characteristics. This discrepancy arises from both the geometric configuration, which significantly differs from 2D to 3D, and the absence of energy dissipation due to friction on the lateral walls (a factor not present in 2D). When we simulate 3D flows with COCD, the avalanche angle aligns with that observed in experiments. For a more detailed discussion, please refer to Sec. V of Ref. [88].

The time evolution of the front velocity v_f, represented in Fig. 11 for simulations, has been shown to be very sensitive to the granular flow behavior [63]. The simulation well reproduces the three main phases observed experimentally in Ref. [64]: an

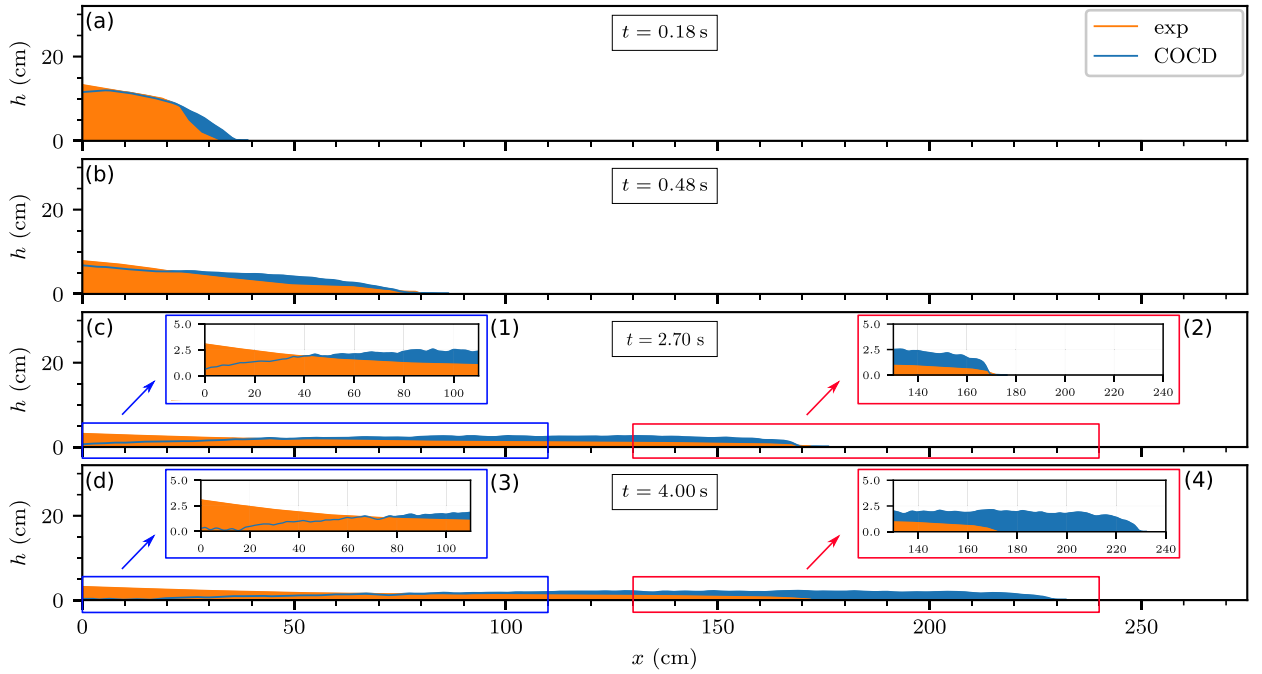

Fig. 10. Profile comparison between 2D simulations and experiments. The aspect ratio is $a = 0.7$ and the slope is $\alpha = 22°$ with an erodible bed of $h_i = 5$ mm.

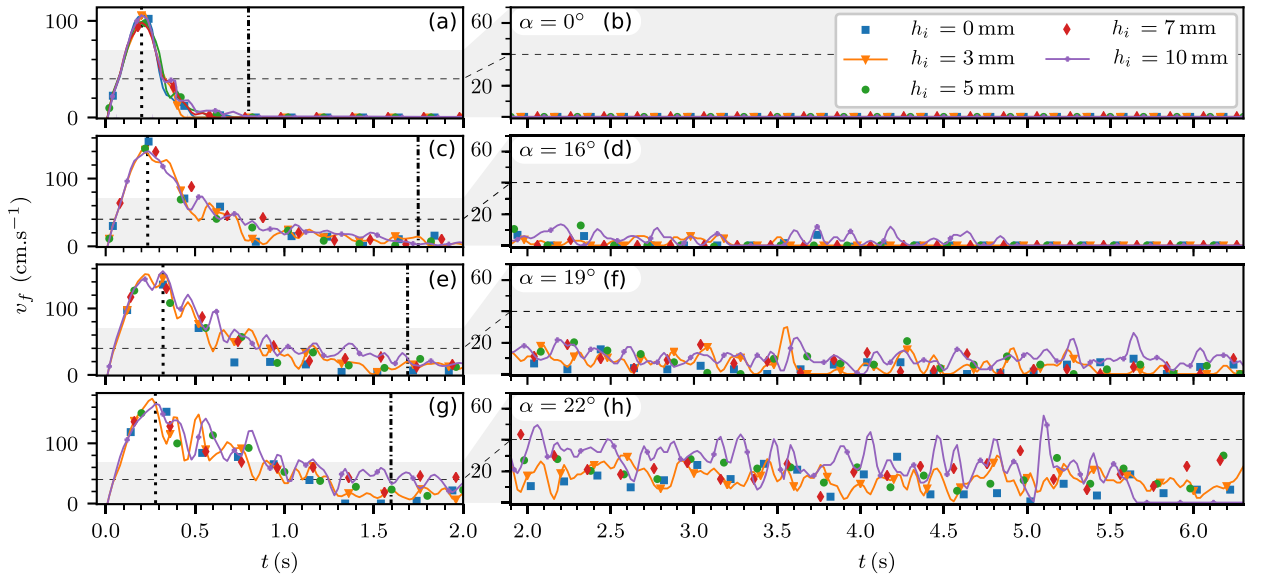

Fig. 11. Evolution of the front velocity of 2D simulations. The results are shown for four inclination angles $\alpha = 0°$ (a,b), $\alpha = 16°$ (c,d), $\alpha = 19°$ (e,f) and $\alpha = 22°$ (g,h), and five bed thicknesses $h_i = 0, 3, 5, 7$, and 10 mm. The second column highlights the slow propagation phase. All simulation parameters can be found in Table A.3, rows 1 to 5.

acceleration phase from the initial time to the time when the front reaches its maximum velocity, a *deceleration phase* from the time when the front velocity is maximal to the beginning of the phase when the front stops decelerating, and a *slow propagation phase* where the flow continues its motion with a velocity fluctuating within a given range that remains roughly constant. The separation between these phases is represented by vertical dashed and dotted-dashed lines, respectively. Furthermore, Fig. 7 of Ref. [64] shows that the slow propagation phase is absent at $\alpha = 0°$, starts to be observed at $\alpha = 16°$, and is well developed at $\alpha = 19°$, in agreement with Figs. 11(a), 11(c), 11(e), and 11(g).

In particular, for $h_i = 10$ mm (purple curve in Fig. 11), the slow propagation phase is clearly observed with front velocities oscillating around 20 cm s^{-1}, which represents 10-15% of the maximum velocity of about 1.6 m s^{-1} in very good agreement with the experiments in Fig. 11 of Ref. [63]. Finally, Figs. 11(a), 11(c), 11(e), and 11(g) show that the thickness of the erodible layer does not

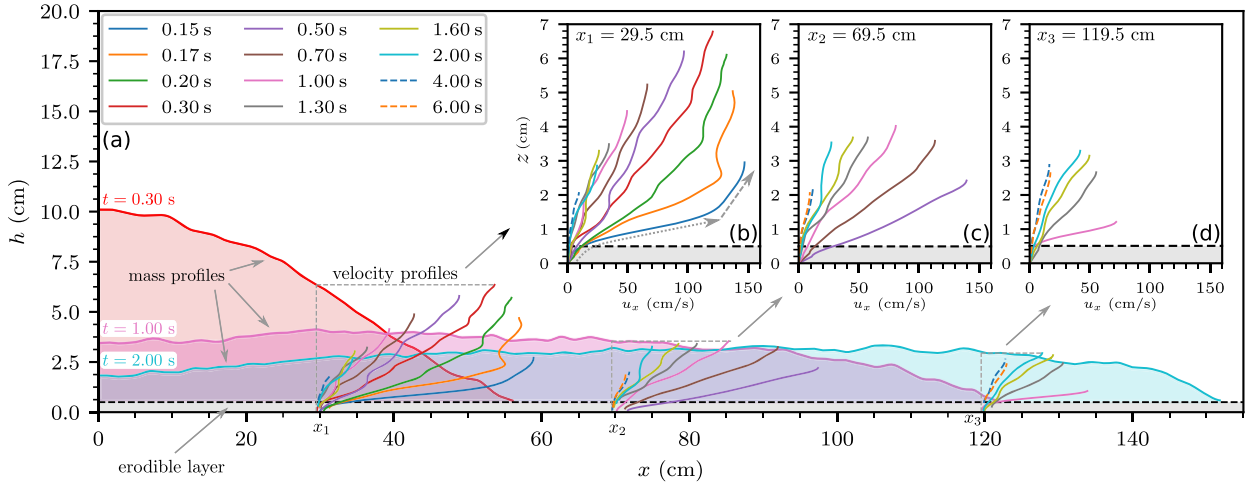

Fig. 12. (a) Velocity profiles at three different positions. Three profiles of the granular mass are represented at times $t = 0.3$ s, $t = 1$ s, and $t = 2$ s corresponding to the flow when the measured free surface elevation is maximal at the positions x_1, x_2, and x_3, respectively. (b-d) Velocity profiles along the flow depth at different times ($t = 0.15$ s to $t = 6$ s) at the three locations along the slope. The horizontal dashed black curve represents the initial erodible layer of thickness $h_i = 5$ mm. The simulation is performed for a slope $\alpha = 22°$ and an initial erodible thickness $h_i = 5$ mm (Table A.3, row 3).

affect the acceleration phase, slightly the deceleration phase but significantly the slow propagation phase (Figs. 11(b), 11(d), 11(f), and 11(h)), in very good agreement with Ref. [63]. Note that the fluctuations of the front velocity also increase with the erodible layer thickness (compare orange and purple curves again).

5.1.2. *Velocity profiles*

Velocity profiles during granular flows have been measured and simulated, in particular for flows on erodible beds [89,75,76]. Such profiles are shown in Fig. 12 for our simulations and can be qualitatively compared to Figs. 15 and 17 of Ref. [75]. The simulation is performed for a slope $\alpha = 22°$ and an initial erodible thickness $h_i = 5$ mm (Table A.3, row 3). Fig. 12(a) represents three sets of velocity profiles at positions $x_1 = 29.5$ cm, $x_2 = 69.5$ cm, and $x_3 = 119.5$ cm, starting at times $t = 0.15$ s, 0.5, and 1 s, respectively, until 6 s. Moreover, a mass profile is represented at times $t = 0.30$ s (red), $t = 1.0$ s (magenta), and $t = 2.0$ s (sky blue), at which the mass thickness $h(x_i)$ is maximum at x_1, x_2, and x_3, respectively. The erodible layer is represented by a horizontal dashed black line, at $h_i = 5$ mm.

The highest velocities are obtained at position x_1. A global decrease of the velocity is observed when moving forward along the horizontal axis (for instance the maximal velocity at probe x_1 is 150 cm s^{-1} (Fig. 12(b)) while it is about 70 cm s^{-1} at x_3 (Fig. 12(d))). At x_1 and for relatively small times $t \lesssim 20$ s, the velocity profiles have an exponential shape from $z = 0$ where the mass is at rest to approximately $z \simeq 1$ cm (see, e.g., the dotted gray arrow in Fig. 12(b)). At later times, the velocity profiles look more like linear functions (at $t = 0.15$, 0.17, 0.2 s in Fig. 12(b)). We clearly observe that the erodible layer has been put into motion (see, e.g., the violet and brown profiles at x_2 (Fig. 12(c)). The arrest phase can also be observed in Figs. 12(b)-(d) where particles near the bed stop before particles near the free surface.

Even though our simulations are in good qualitative agreement with experiments, quantitative comparisons are more difficult as shown in Fig. 13 representing the downslope velocity profiles u_x at $x = 110$ cm. The dotted curves represent experimental data measured in Ref. [64] and extracted first in Ref. [76] while the continuous curves represent our simulations. The time starts ($t = 0$ s) when the front reaches the position x. Good agreement is observed at this initial time, corresponding to the front arrival. For larger times, significant differences between simulations and experiments can be observed. On the other hand, the maximum velocity and the free surface elevation are roughly well reproduced by the simulations for $t \lesssim 0.8$ s. The main difference is in the static/flowing transition that rises towards the free surface in the experiments while staying roughly at the surface of the erodible layer in the simulations. This is partly explained by the absence of wall effects in 2D simulations. Indeed the additional dissipation related to lateral friction with the walls induces a thicker basal static layer as shown in continuum simulations (see, e.g., Fig. 4 of Ref. [19]).

Erosion processes and associated energy transfer between the flowing grains and the initially static grains of the erodible bed are highlighted in Fig. 14 which represents the kinetic to potential energy ratio of the erodible bed e_k (normalized by its maximum value $\|e_k\|_\infty$ in Fig. 14), defined by

$$e_k = \frac{E_k(\text{bed})}{E_p(\text{bed})},$$

where E_k(bed) and E_p(bed) are respectively the kinetic and potential energies of the bed. Erosion clearly increases with the slope angle α (compare the maximal values reached in Figs. 14(a)-(c)) and with the bed thickness. Note that at 22°, the kinetic energy of the erodible bed at $h_i = 7$ mm (red curve) is larger than at $h_i = 10$ mm (purple curve) during the first 1.5 s (Fig. 14(c)). This phenomena has also been observed in the experiments (see blue curve with diamonds in Fig. 9(b) of Ref. [64] where the runout

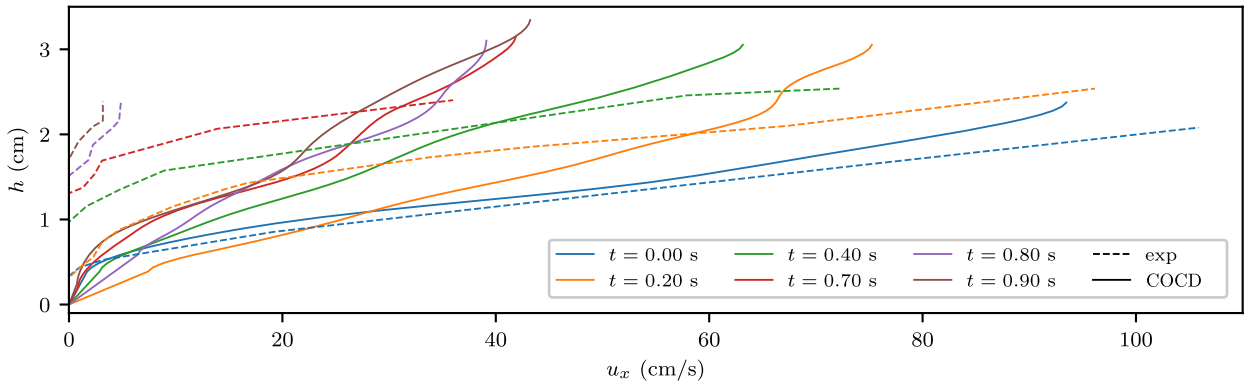

Fig. 13. Comparison between velocity profiles obtained by our simulations and profiles obtained by experiments. In this figure, the time $t = 0$ s corresponds precisely to the time when the front reaches the position $x = 110$ cm. The velocity profiles are measured starting at this time. The simulation is performed for a slope $\alpha = 22°$ and an initial erodible thickness $h_i = 5$ mm (Table A.3, row 3).

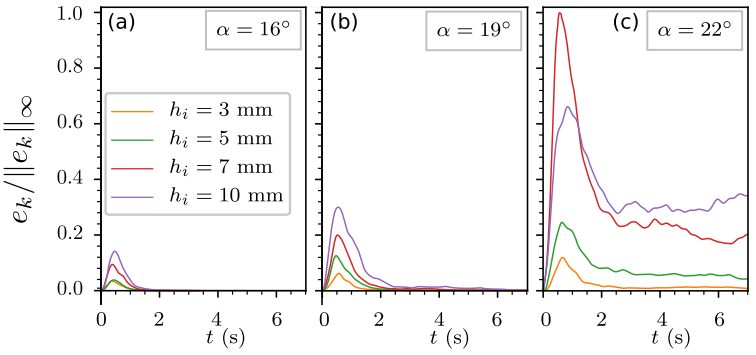

Fig. 14. Normalized kinetic energy of the erodible bed. Simulations are performed on three slopes (a) $\alpha = 16°$, (b) $\alpha = 19°$, and (c) $\alpha = 22°$ for erodible beds $h_i = 3$, 5, 7, and 10 mm. The simulation parameters can be found in Table A.3, rows 2 to 5.

distance saturates and even decreases when h_i exceeds 12 particles). This could be explained by the energy lost in moving the grains deep in the bed without significant down-slope motion of these deep particles. At $t > 1.5$ s, the purple curve ($h_i = 10$ mm) is higher than the red one ($h_i = 7$ mm), as observed for smaller angles in Figs. 14(a,b). This is again in very good agreement with experiments (see green and blue curves in Figs. 9(a)-(b) of Ref. [64]).

5.1.3. Wave motion

In Ref. [64], erosion waves were observed near the flow head, highlighting the exchange processes between the flow and the erodible bed. Such instabilities can occur when two fluids with different velocities and densities move one above the other. If the flowing layer and the erodible layer can be assimilated to two different fluids with different densities and distinct down-slope velocities, a slight perturbation at the interface can be amplified by the local velocity difference and the local decrease in flow pressure. If the velocity of the superjacent fluid is sufficient, the amplified perturbation can transform into a breaking wave [10,64].

The authors of Ref. [64] suggested that the wave-like motion they observed can be assimilated to Kelvin-Helmholtz instabilities. However, due to the experimental nature of their study, it was challenging for them to measure certain quantities such as density differences within the flow and then to confirm their intuition. They used order-of-magnitude calculations to verify that the instability conditions are well satisfied. Since we also observe such waves in our numerical simulations (Fig. 15), we use our outputs to access these measurements, and we show that the conditions for the formation of Kelvin-Helmholtz instabilities are indeed well fulfilled, confirming their intuition.

The criterion developed by Rowley et al. (2011) [10] provides a threshold for the minimum velocity difference $u_1 - u_2$ between the upper (1) and lower (2) layers that is necessary for the growth of Kelvin-Helmholtz instabilities. For a given wavelength λ, this criterion is expressed by equation

$$u_1 - u_2 \geq \sqrt{\frac{g\lambda}{2\pi}\left(\frac{\Phi_2}{\Phi_1} - \frac{\Phi_1}{\Phi_2}\right)},$$

where g is the gravity field and Φ is the granular volume fraction. In the experiments conducted in Ref. [64], the calculated velocity difference is $u_1 - u_2 \simeq 0.4$ m s^{-1} for the specific case of granular flows at $\alpha = 22°$, $V = 12\,600$ cm^3, $a = 0.7$, $\lambda \simeq 7$ cm (see Fig. 20 in

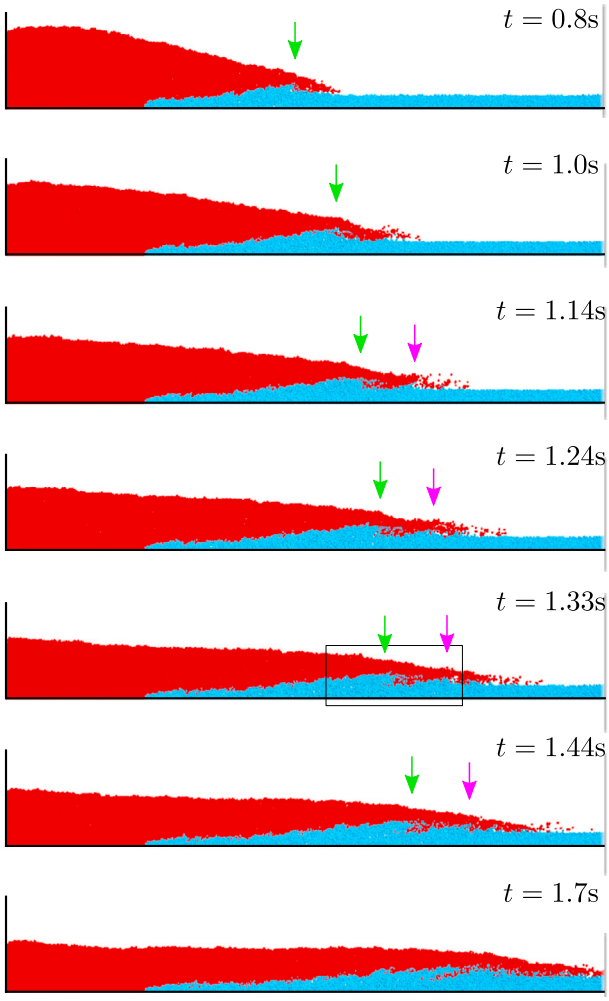

Fig. 15. Snapshots at different times. The red grains are initially from the column and the blue grains from the bed. The simulation parameters can be found in Table A.3, row 6. The slope is $\alpha = 22°$.

Ref. [64]), and $\Phi_1 \simeq 6400$ grains per cm^3 that is $\Phi_1 \simeq 0.8\,\Phi_2$. The values of Φ_1, Φ_2, and λ have been roughly estimated in these experiments.

In our numerical experiment, the ratio between Φ_1 and Φ_2 is also about 0.8 (Fig. 16(a)) and the wavelength λ is about 8 cm (Fig. 16(c)), close to the estimations in Ref. [64]. These values lead to a minimum velocity difference $u_1 - u_2 \simeq 0.24$ m s^{-1}. The criterion to observe Kelvin-Helmholtz instabilities is thus fulfilled in our simulations since the velocity difference between the two layers is much higher (compare the values of u_x in Fig. 16(b)). Indeed, the flowing layer (above the black dashed curve) has a typical down-slope velocity higher than 0.40 m s^{-1} while the velocity of the erodible layer stays under 0.15 m s^{-1}.

Note that the analogy with Kelvin-Helmholtz instabilities is validated only at the flow head because such well-developed instabilities require a velocity difference to be maintained between the two fluids, explaining why the instabilities vanish when the flowing mass slows down. In the experiments as well as in the simulations, the velocity difference is sufficiently high only at the flow head and during a relatively short time (in simulations, they can be observed between 0.9 and 2.2 s). In experiments, the waves are indeed observed mostly in the flow head and when the front velocity exceeds 0.4 m s^{-1}.

Furthermore, Fig. 16(c) shows that grain geometrical arrangements within the erodible layer create obstacles acting into the erosion process. In Fig. 16, the velocity vectors of grains belonging to the erodible layer are represented by the black arrows. The zone below the red curve represents the portion of the erodible bed where the grains are quasi-static at $t = 1.33$ s. Two stacks of particles are shown between $x = 48$ and 53 cm and $x = 60$ and 65 cm (between the red vertical dotted lines). The flowing particles from the erodible bed appear to encounter these two stacks, contributing to the wave-like oscillations. This wave-like motion has a signature during the flow on the free surface, as observed in the experiments of Ref. [63] (see their Figs. 19 and 20). However, in the deposit, there is no clear signature of these waves in our simulations since they disappear as the flow decelerates, aligning with observations in the experiments of Refs. [63,10,90,64].

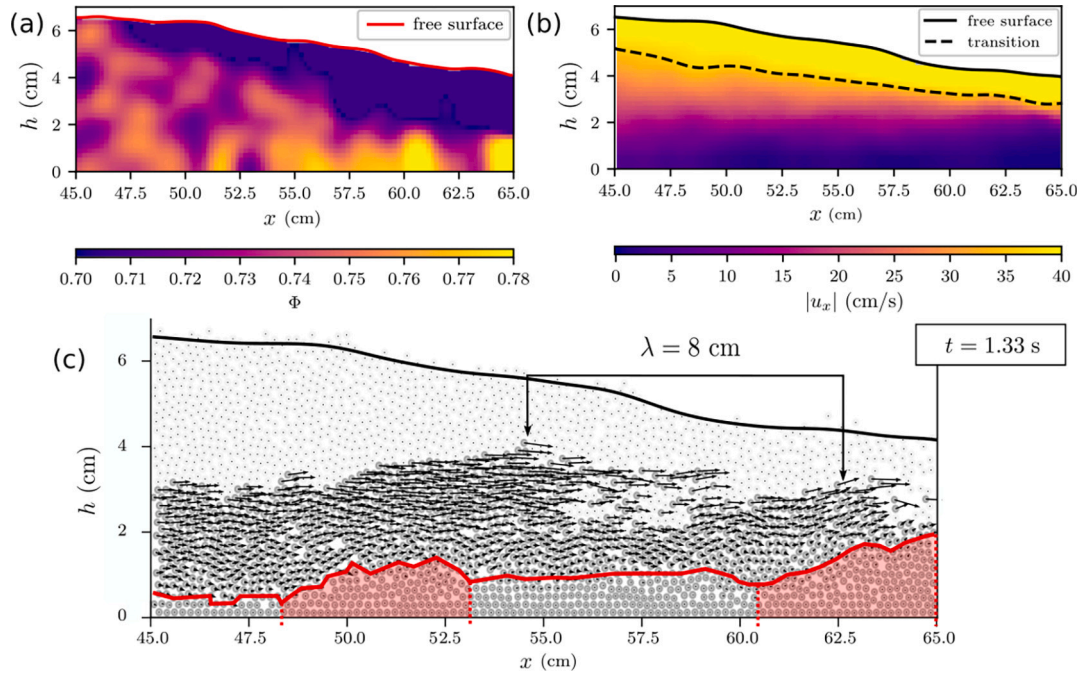

Fig. 16. Wave motion characteristics near the front at $t = 1.33$ s. The slope is $\alpha = 22°$ (see Table A.3, row 6). (a) Difference between Φ_1, the solid volume fraction of the flowing layer, and Φ_2, the solid volume fraction of the erodible bed. (b) Difference of downslope velocities between the flowing layer and the erodible layer, arbitrarily separated by a dashed black curve. (c) Granular profile and velocity vectors (black arrows) of each particle of the erodible layer. The wave motion can be identified visually with a wavelength of approximately 8 cm. The grains below the red curve are quasi-static.

5.2. 3D simulations: static/flowing transition and compaction effects

5.2.1. Effect of initial solid volume fraction

Initial compaction and associated dilatancy effects may change the behavior of dry granular flows [91–93] even though this effect is more dramatic in the presence of a fluid [94]. For instance, for identical volumes, an initially compacted mass released on a compacted bed spreads less than a compacted mass on a loose bed [64]. It is expected that the initial compaction of the erodible layer will change the depth at which the flow will put the beads of the erodible bed into motion. We therefore investigate the simulated evolution of the static/flowing transition that we qualitatively compare with the experimental observations given in Ref. [64]. This transition that we denote h_{sf} corresponds to the thickness of the static layer within the initial erodible bed.

Three simulations were performed, with identical parameters (see Table A.3), except for the initial solid volume fraction. The compaction was modified when preparing the initial granular column and erodible bed by changing the value of the friction coefficient between grains. The initial mass is built up through a uniform rain. This process leads to a pressure field on the ground with qualitatively hydrostatic profiles [95]. In our simulations, the initial compaction is then a function of the friction coefficient μ used to prepare the initial set-up.

We refer to these three simulations as follows: *loose/loose* when both the column and the bed are built with a friction coefficient $\mu = 0.3$, *compact/compact* when both the column and the bed are built without friction ($\mu = 0$), and *compact/loose* when the granular column is built with $\mu = 0$ and the granular bed with $\mu = 0.3$. An example of an initial set-up can be found in Fig. 17(a) for the *compact/loose* simulation. In these simulations, the aspect ratio is $a = H/L = 0.7$, with a granular bed elevation of $h_i = 5$ mm corresponding approximately to five sphere diameters and a channel width $W = 0.8$ cm, corresponding approximately to ten sphere diameters. All parameters can be found in Table A.3, rows 7 to 9, at corresponding names. Note that in these simulations, there is a layer of glued beads on the rigid plane under the erodible bed.

In the experiments of Ref. [64], relatively similar grain sizes, plane slopes, initial bed elevations, and aspect ratios are used. However, the volumes are quite different since the dimensions of the flowing mass at the initial time is a box of dimensions $H_0 \times R_0 \times W = 14 \times 20 \times 20$ cm^3, involving approximately 9 million spheres. Since our computational capacities cannot handle such number of spheres, we reduced the box dimensions by two and dramatically decrease the channel width W, leading to a simulated mass dimension of $H_0 \times R_0 \times W = 10.0 \times 7.0 \times 0.8$ cm^3. Shortening the channel width and lowering the initial volume of the column is known to reduce mass entrainment leading to a smaller runout distance [64]. However, in such a narrow channel, the flow will be significantly influenced by the lateral walls. Thus, to minimize wall effects, which will be much higher in our simulations than in experiments since our channel is much narrower, we set $\mu = 0$ for all grain/wall interactions. For a detailed analysis of the effects of side walls in laboratory experiments and numerical simulations, refer to Refs. [19,63,64,77].

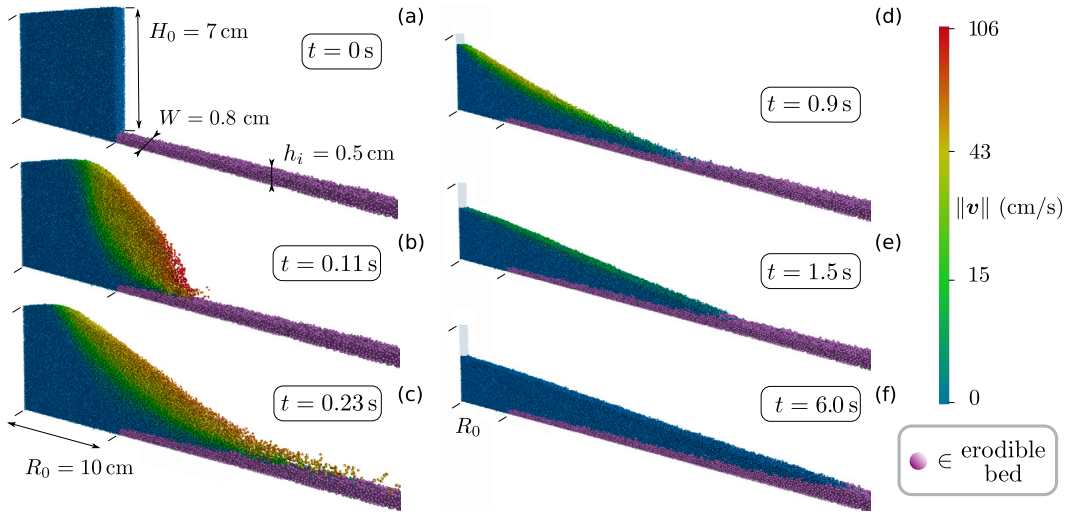

Fig. 17. Snapshots of the *compact/loose* simulation. The parameters of this 3D simulation can be found in Table A.3, row 7. The initial column dimensions are $R_0 \times H_0 \times W = 10 \times 7.0 \times 0.8\,\text{cm}^3$. The erodible thickness is about 0.5 cm, corresponding to five mean grain parameters $d = 1.0$ mm. The purple spheres belong to the initial erodible bed. This simulation involves $N = 122\,434$ grains and the slope is $\alpha = 22°$. The mass is at rest in Fig. f at $t = 6.0$ s. The three main phases are represented here: the acceleration (a) and (b), deceleration (c), and slow propagation phase (d), (e), and (f).

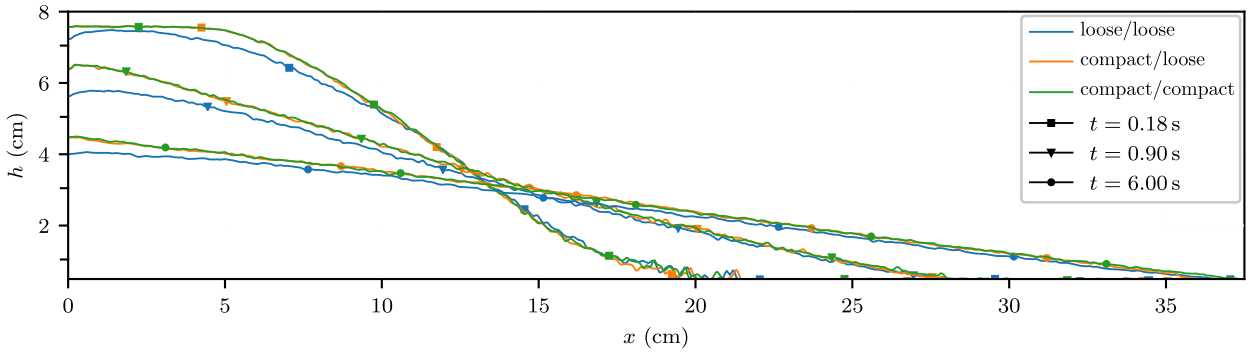

Fig. 18. Profile comparison for different compactions. The slope is $\alpha = 22°$ and the bed thickness is $h_i = 5$ mm (five grains of mean diameter; see Table A.3, rows 7 to 9). There are no notable differences in front position. However, it can be seen that the maximal height at $x = 0$ cm is smaller in the loose case. This is probably caused by a compaction of the column during its collapse.

Fig. 18 shows that the initial compaction in our simulations does not change the runout distance. Indeed, the compaction of the initial column mainly changes the upstream mass profiles as was observed in the DEM and continuum simulations of Refs. [91,93]. The upstream thickness of the initially compact column is larger than for the initially loose column.

5.2.2. *Static/flowing interface and velocity profiles*

Fig. 19, which must be studied in parallel to Fig. 17 in Ref. [64], highlights the evolution of three main quantities: the front velocity v_f as a function of the space position x (Fig. 19(a)), the time evolution of the static/flowing transition elevation h_{sf}, (Figs. 19(b)-(f)), and the horizontal mean velocity u_x as a function of the normal elevation to the plane z (Figs. 19(g)-(k)). The static/flowing transition h_{sf} is defined by a criterion on the value of the downslope velocity u_x as follows: $h_{sf} := \min z(x)$, such that $0 \le z(x) \le h_i$ and $u_x(z) \le c$, where h_i represents the initial granular bed elevation (here about five mean sphere diameters $h_i = 5d$), and $c = 1$ cm s^{-1}, as in Ref. [64].

In Fig. 19(a), the three main phases defined in Sec. 5 can be distinguished in the evolution of v_f. On the contrary, the acceleration phase (see, e.g., the snapshots a and b in Fig. 17 for *compact/loose*) is quite independent of compaction of the granular mass and bed, from approximately $x = R_0 = 10$ cm to $x \simeq 16$ cm. The maximal front velocity is about 75 cm/s at $x = 16$ cm. The deceleration phase (Fig. 17(c)), observed from $x = 16$ cm to 26.5 cm, significantly depends on the compactness of the initial set-up (Fig. 19(a)). The smallest deceleration (i.e. highest velocities) is observed in the *compact/compact* simulation (orange curve) which is the only case where the erodible layer is compact. This could be related to the smaller dissipation of moving grains in the deep part of the erodible bed compared to the loose bed. For flows on a loose bed, the loose column front (*loose/loose* simulation) decelerates less than the compact column (*compact/loose* simulation) for front positions up to about 20 cm and then decelerates more (the blue curve drops below the green curve). The slow propagation phase (Figs. 17(d), 17(e) and 17(f)) characterized by a quasi-steady small front

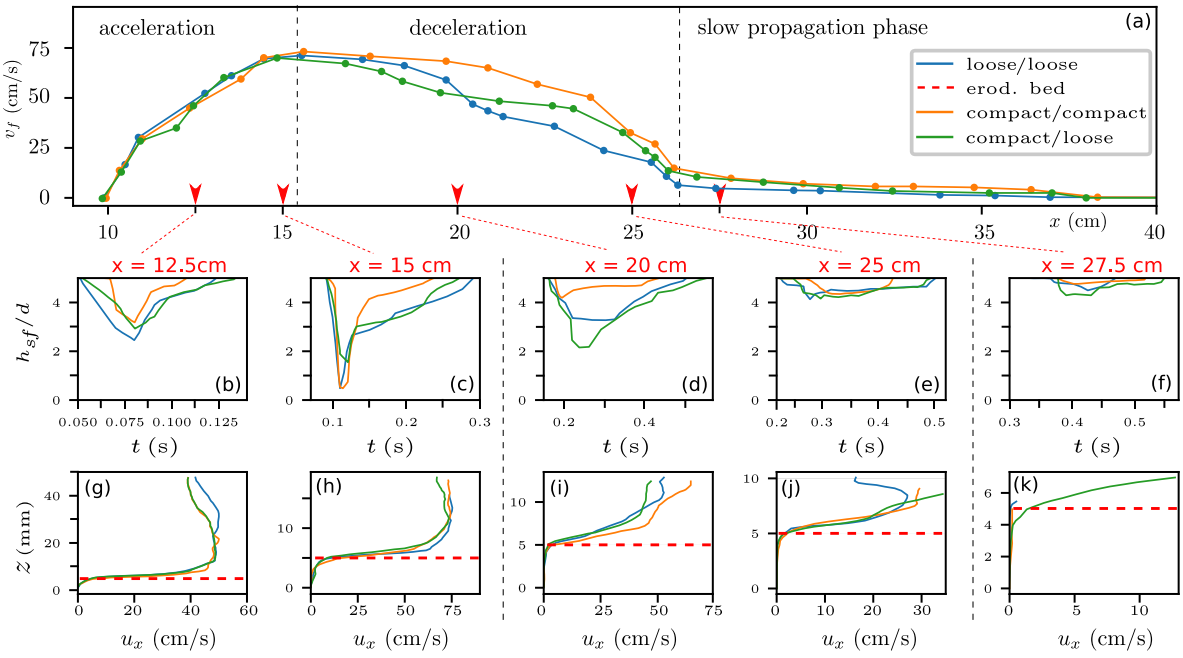

Fig. 19. Velocity profiles and time evolution of the static/flowing transition. The slope is $\alpha = 22°$ and the bed thickness is $h_i = 5$ mm (five grains of mean diameter). There are five points where measurement have been performed. Two in the acceleration phase x_1, x_2, two in the deceleration phase x_3, x_4, and one more in the slow propagation phase x_5. Simulation parameters can be found in Table A.3, rows 7 to 9, named *compact/loose, loose/loose* and *compact/compact*. In the third row, we represent the downslope velocity in the granular media at a given position x. These velocities have been measured at time t^0 at which the transition h_{sf} has reached its minimal value (meaning that the static/flowing transition is the deepest in the erodible layer).

velocity starts at $x = 26.5$ cm with $v_f \simeq 15$ cm s^{-1} (Fig. 19(a)). In this phase, the velocity of the compact column and bed is still higher than the front velocity of the compact column on a loose bed, itself higher than in the loose column and bed case.

The time evolution of the transition h_{sf} is represented in Figs. 19(b)-(f). We measured it at two points in the acceleration phases: $x = 12.5$ and 15 cm, two others in the deceleration phase $x = 20$ and 25 cm and another one in the slow propagation phase $x = 27.5$ cm. Note that the point where the maximal velocity of the front has been measured is $x = 15$ cm. In our simulations, three typical behaviors can be observed depending on the considered phase.

In the acceleration phase, the penetration of the static/flowing interface h_{sf} within the erodible bed is sharp, reaching the deeper position very quickly (e.g., at $t = 0.1$ s in Fig. 19(c)). The interface elevation then increases (i.e., rises) until the value of the initial bed thickness $h_i = 5d$. Furthermore, it can be observed that for faster velocities, the interface seems to penetrate deeper (note the value of v_f in Fig. 19(a) and of h_{sf} in Figs. 19(b)-(f)). We also observe that the granular bed stabilizes more rapidly when it is initially compact. In the deceleration phase, the change of the interface elevation h_{sf} is smoother than in the acceleration phase and its minimal value is smaller (compare Figs. 19(d,e) with Figs. 19(b,c)). The biggest difference between the curves is observed at $x = 20$ cm with a smaller penetration of the static/flowing interface h_{sf} in the *compact/compact* case, followed by the *loose/loose* and *compact/loose* cases. The static/flowing interface h_{sf} penetrates deeper at position $x = 20$ cm (the middle of the deceleration phase) than those at $x = 25$ cm, (the end of this phase). At this latter position, the penetration is almost the same whatever the initial compaction while the duration of the motion of grains in the erodible bed is smaller for flows on a compact bed (orange curve). During the slow propagation phase, differences similar to those observed at $x = 20$ cm between the curves start to become visible again (Fig. 19(f)).

In the third row of Fig. 19, we represent the downslope velocity in the granular media at a given position x. These velocities have been measured at time t^0 where the transition h_{sf} has reached its minimal value (meaning that the static/flowing transition is the deepest in the erodible layer). For example, the velocity profile shown in Fig. 19(h) has been measured at $t = 0.11$ s, when h_{sf} is the smallest in Fig. 19(c).

During the acceleration phase Figs. 19(g,h), we observe profiles as in Fig. 12(b) at $t = 0.15$ s decomposed into an exponential shape around the erodible bed surface $z \simeq 5$ mm connecting above to a roughly constant velocity up to the free surface. Surprisingly, Figs. 19(g,h) show that the downslope velocity is maximal in the middle of the granular layer at the initial instants, as observed, e.g., in Fig. 17(b) for the *compact/loose* case. This maximum velocity is about 75 cm s^{-1} and is obtained when the front velocity is maximal (also about 75 cm s^{-1}), as shown in Fig. 19(a) at $x = 16$ cm. Note that this value is about two times smaller than the maximal velocity of the fastest spheres that move at about 1.5 m/s. These high-speed spheres are located slightly above the free surface and have a collision behavior. In the deceleration phase, roughly linear velocity profiles are observed in Figs. 19(i,j), except for *loose/loose* at $x = 25$ cm (blue curve), which is still similar to profiles from the acceleration phase. At $x = 20$ cm, the downslope velocity is still relatively high, similar to the front velocity (Fig. 19(i)). These velocities get globally smaller at $x = 25$ cm. During the

slow propagation phase, the only significant velocity is obtained for the *compact/loose* case with a maximum of 12 cm s^{-1} within a very thin layer of flowing particles.

5.2.3. Insight into erosion process

During the mass acceleration, the flow interaction with the erodible bed is quick and highly energetic since the flow velocity is high. This leads to profound rearrangements in the granular bed (Figs. 19(b,c)) with deep particles put into motion. However, the short-duration of this interaction leads to relatively small mass entrainment in the down-slope direction compared to what happens during the deceleration phase. For example, the erosion process lasts 0.1 and 0.2 s in Figs. 19(a,b), respectively, compared to 0.45 and 0.35 s in Figs. 19(d,e), respectively.

During the deceleration phase, the interface seems to stay approximately in the middle of the bed (Figs. 19(d,e)). The most important part of the mass that is displaced belongs to the first upper half of the granular bed. Beyond $x = 26$ cm, the mass flows on the erodible bed without significant entrainment (the maximal depth of the static/flowing interface is about one diameter only (Fig. 19(f)). During these three phases, the initial solid volume fraction plays a role in the dynamics, especially in the evolution of the static/flowing interface h_{sf}, which penetrates deeper within the loose erodible bed. Despite the difference in the dynamics for flows on a loose or compact bed, the runout distance is almost unaffected.

When comparing our observations with those given in Ref. [64], a lot of similarities can be found. The same three phases are observed along with the main characteristics of the static/flowing interface evolution and velocity profiles, at least qualitatively but also partly quantitatively. However, as expected from the different geometry of the domain, the precise values of velocity and interface thicknesses differ. For example, the static/flowing interface h_{sf} in the experiments is systematically deeper than in the simulations. Unfortunately, our computational capacities prevent us from reproducing exactly the experiments (number of grains and dimensions of the set-up). As mass entrainment decreases with smaller volumes of the granular mass and narrower channel width W [63,64], the differences between our simulations and the experiments lie in the good direction since our simulations involve a lower volume and a narrower channel.

6. Conclusion

In this article, we have presented the COCD method that simulates the motion of each grain and the complex interactions between them. It belongs to the Discrete Elements Methods, in particular to the convexified contact dynamics methods (CM) [51–61]. Indeed, in COCD, the computation of the numerical solution involves solving a convex optimization problem at each time step, based on the global velocity as the unknown. After explaining the method, describing its implementation in the MOSEK solver (with its Primal-Dual Interior Point Method) and its calibration, we validated COCD by confronting it with experiments and the non-convex contact dynamics method NSCD [48,49,47]. We finally tested COCD in the context of granular flows on erodible beds.

Our article demonstrates the interest of the convexified contact dynamics methods for three main reasons:

- From a theoretical point of view, a high level of confidence can be given to the numerical result. In this respect, we have presented theoretical results for a convexified scheme based on the full circular Coulomb cone and a velocity-based optimization formulation. It certifies that Coulomb's law is well verified locally at each contact and at each iteration in time.
- From a computational performance point of view, the efficiency of COCD is derived from existing convex solvers, benefiting from the performance gains obtained in this research field (see, e.g., the algorithms presented in Refs. [56–61]).
- Convexified methods have already proven efficient in various engineering fields (see, e.g., Refs. [96,97]). This article advocates for their relevance in the field of geophysical sciences. Indeed, our tests of COCD in the context of granular flows on erodible beds show that COCD reproduces qualitative and many quantitative features of laboratory experiments such as erosion processes associated with the complex interaction between a flowing and a static layer. However, particular attention should be paid when comparing 2D simulations conducted with COCD to 3D flow experiments. Indeed, when the inclination of the plane is greater than 16°, 2D COCD simulations tend to strongly overestimate the runout distance of the flow and will never stop since the effective avalanche angle of 2D discrete element simulations is smaller than that of 3D simulations with the same inter-particle friction.

In conclusion, we showed that the convexified method COCD is suitable for reproducing physical phenomena involving granular flows at the laboratory scale. Such validation steps are essential because the models can then be trusted to access quantities that could be very difficult to measure in laboratory experiments, like, for example, velocity fields, static fluid transitions, and flow interaction with the erodible bed within the domain.

CRediT authorship contribution statement

Hugo A. Martin: Conceptualization, Methodology, Software, Writing – original draft, Writing – review & editing. **Anne Mangeney:** Conceptualization, Funding acquisition, Methodology, Project administration, Supervision, Writing – original draft, Writing – review & editing. **Aline Lefebvre-Lepot:** Conceptualization, Methodology, Supervision, Writing – original draft. **Bertrand Maury:** Conceptualization, Methodology, Supervision, Writing – original draft. **Yvon Maday:** Conceptualization, Funding acquisition, Methodology, Project administration, Supervision, Writing – original draft.

Declaration of competing interest

The authors declare that they have no known competing financial interests or personal relationships that could have appeared to influence the work reported in this paper.

Data availability

Data will be made available on request.

Acknowledgements

This article has been funded by the ERC Contract No. ERC-CG-2013-PE10-617472 SLIDEQUAKES. The simulations were performed with two Intel Xeon E5-2650 2.00 GHz (2×8 cores) processors on the S-CAPAD platform, IPGP, France. We thank MOSEK ApS [79] for the free academic license that made this article possible. We warmly thank Lydie Staron for providing us with her simulation data, and Jean-Pierre Vilotte for the discussions that led to the completion of this work.

Appendix A. Simulation parameters

Tables A.2 and A.3 presented in this Appendix contain all the parameters necessary for the reproducibility of our numerical simulations.

Table A.2
Simulation parameters for computational aspects and comparison with NSCD and experiments. The units of quantities in the table are: H_0, R_0, W (cm), α (°), Δt (s), d (mm), t_f (s). The other parameters are unitless. In all our simulations, the gravity constant is $g = 9.81\ \mathrm{m\,s^{-2}}$, the grain density is $\rho = 2\,500\ \mathrm{kg\,m^{-3}}$ and there is a polydispersity of 10% for grains size. The friction coefficient with the walls is μ. The last two rows provide information about the experiments. Any empty cell is equal to the cell value of the row above.

		initial column dimensions $R_0 \times H_0 \times W$ (cm × cm × cm)	aspect ratio a	number of particles N (grain)	slope α (°)	friction coefficient μ	time step Δt (s)	mean diameter of grains d (mm)	final time t_f (s)
1	*variation of* Δt	15×15	1.0	952	0	0.3	$0.01 \rightarrow 5.0\,10^{-5}$	7.0	0.5
2	*variation of* N			$500 \rightarrow 50\,000$			0.001	$7.6 \rightarrow 0.78$	3.0
3	*comparison with NSCD*	10.8×71.928	6.66	7 740		0.5		5.0	2.0
4	*variation of* μ	$20 \times 14 \times 20$	0.7	112 459		$0.0 \rightarrow 0.8$	0.01	4.0	2.04
5	2D	20×14	0.7	2 154	0, 22	0.3	0.01	4.0	2.04
6	3D	$20 \times 14 \times 20$		112 459					
7	*M2010*	$20 \times 14 \times 10$	0.7	$\simeq 9\ 10^6$	0	/	/	0.7	/
8	*F2014*	$20 \times 14 \times 20$							

Table A.3
Simulation parameters for simulations with erodible beds. The units of quantities in the table are: H_0, R_0, W (cm), α (°), Δt (s), d (mm), t_f (s). The other parameters are unitless. In all our simulations, the gravity constant is $g = 9.81\ \mathrm{m\,s^{-2}}$, the grain density is $\rho = 2\,500\ \mathrm{kg\,m^{-3}}$ and there is a polydispersity of 10% for grains size. The friction coefficient with the walls is μ, except for simulations in 3D where the walls are frictionless (*compact/loose*, *loose/loose*, and *compact/compact*). Any empty cell is equal to the cell value of the row above.

		dimension	initial column dimensions $R_0 \times H_0 \times W$ (cm × cm × cm)	bed width h_i (mm)	slope α (°)	number of particles N (grain)	friction coefficient μ	time step Δt (s)	mean diameter of grains d (mm)	final time t_f (s)
1	*erodible beds*	2D	20×14	0	0, 16, 19, 22	19 621	0.9	0.001	1.0	6.5
2				3		28 884				
3				5		34 059				
4				7		37 254				
5				10		44 996				
6	*erosion waves*	2D	20×14	20	22	33 374	0.9	0.001	1.8	6.5
7	*compact loose*	3D	$10 \times 7 \times 0.8$	0.7	22	122 434	0.3	0.01	1.0	6.0
8	*loose loose*					122 012				
9	*compact compact*					122 932				
10	*F2014erod*	3D	$20 \times 14 \times 20$	3,5,7	16, 19, 22	/	/	/	0.7	/

References

[1] R. Delannay, A. Valance, A. Mangeney, O. Roche, P. Richard, Granular and particle-laden flows: from laboratory experiments to field observations, J. Phys. D, Appl. Phys. 50 (5) (2017) 53001, https://doi.org/10.1088/1361-6463/50/5/053001.

[2] A. Lucas, A. Mangeney, J.P. Ampuero, Frictional velocity-weakening in landslides on Earth and on other planetary bodies, Nat. Commun. 5 (1) (2014) 3417, https://doi.org/10.1038/ncomms4417.

[3] A. Lucas, A. Mangeney, Mobility and topographic effects for large Valles Marineris landslides on Mars, Geophys. Res. Lett. 34 (10) (2007) L10201, https://doi.org/10.1029/2007GL029835.

[4] J. Dufek, T. Esposti Ongaro, O. Roche, Pyroclastic density currents, in: H. Sigurdsson (Ed.), The Encyclopedia of Volcanoes, second ed., Academic Press, Amsterdam, the Netherlands, 2015, pp. 617–629, https://linkinghub.elsevier.com/retrieve/pii/B9780123859389000353.

[5] S. Utili, T. Zhao, G.T. Houlsby, 3D DEM investigation of granular column collapse: evaluation of debris motion and its destructive power, Eng. Geol. 186 (2015) 3–16, https://doi.org/10.1016/j.enggeo.2014.08.018.

[6] F. Guzzetti, Invited perspectives: landslide populations – can they be predicted?, Nat. Hazards Earth Syst. Sci. 21 (5) (2021) 1467–1471, https://doi.org/10.5194/nhess-21-1467-2021.

[7] A. Guimpier, S.J. Conway, A. Mangeney, A. Lucas, N. Mangold, M. Peruzzetto, M. Pajola, A. Lucchetti, G. Munaretto, T. Sæmundsson, A. Johnsson, L. Le Deit, P. Grindrod, J. Davis, N. Thomas, G. Cremonese, Dynamics of recent landslides (<20 My) on Mars: insights from high-resolution topography on Earth and Mars and numerical modelling, Planet. Space Sci. 206 (2021) 105303, https://doi.org/10.1016/j.pss.2021.105303.

[8] M.J. Froude, D.N. Petley, Global fatal landslide occurrence from 2004 to 2016, Nat. Hazards Earth Syst. Sci. 18 (8) (2018) 2161–2181, https://doi.org/10.5194/nhess-18-2161-2018.

[9] P. Poulain, A. Le Friant, R. Pedreros, A. Mangeney, A.G. Filippini, G. Grandjean, A. Lemoine, E.D. Fernández-Nieto, M.J. Castro Díaz, M. Peruzzetto, Numerical simulation of submarine landslides and generated tsunamis: application to the on-going Mayotte seismo-volcanic crisis, C. R. Géosci. 354 (S2) (2023) 361–390, https://doi.org/10.5802/crgeos.138.

[10] P.J. Rowley, P. Kokelaar, M. Menzies, D. Waltham, Shear-derived mixing in dense granular flows, J. Sediment. Res. 81 (12) (2011) 874–884, https://doi.org/10.2110/jsr.2011.72.

[11] B. Sovilla, P. Burlando, P. Bartelt, Field experiments and numerical modeling of mass entrainment in snow avalanches, J. Geophys. Res., Earth Surf. 111 (F3) (2006) F03007, https://doi.org/10.1029/2005JF000391.

[12] T. Borykov, D. Mège, A. Mangeney, P. Richard, J. Gurgurewicz, A. Lucas, Empirical investigation of friction weakening of terrestrial and Martian landslides using discrete element models, Landslides 16 (6) (2019) 1121–1140, https://doi.org/10.1007/s10346-019-01140-8.

[13] D.-H. Nguyen, É. Azéma, P. Sornay, F. Radjaï, Rheology of granular materials composed of crushable particles, Eur. Phys. J. E 41 (4) (2018) 50, https://doi.org/10.1140/epje/i2018-11656-1.

[14] A. Mangeney, L. Staron, D. Volfson, L. Tsimring, Comparison between discrete and continuum modeling of granular spreading, WSEAS Trans. Math. 2 (6) (2006) 373–380, https://www.ipgp.fr/~mangeney/wseas.pdf.

[15] E.C.P. Breard, L. Fullard, J. Dufek, M. Tennenbaum, A. Fernandez Nieves, J.F. Dietiker, Investigating the rheology of fluidized and non-fluidized gas-particle beds: implications for the dynamics of geophysical flows and substrate entrainment, Granul. Matter 24 (1) (2022) 34, https://doi.org/10.1007/s10035-021-01192-5.

[16] H.M. Jaeger, S.R. Nagel, R.P. Behringer, Granular solids, liquids, and gases, Rev. Mod. Phys. 68 (4) (1996) 1259, https://doi.org/10.1103/RevModPhys.68.1259.

[17] P.Y. Lagrée, L. Staron, S. Popinet, The granular column collapse as a continuum: validity of a two-dimensional Navier-Stokes model with a μ(I)-rheology, J. Fluid Mech. 686 (2011) 378–408, https://doi.org/10.1017/jfm.2011.335.

[18] I.R. Ionescu, A. Mangeney, F. Bouchut, O. Roche, Viscoplastic modeling of granular column collapse with pressure-dependent rheology, J. Non-Newton. Fluid Mech. 219 (2015) 1–18, https://doi.org/10.1016/j.jnnfm.2015.02.006.

[19] N. Martin, I.R. Ionescu, A. Mangeney, F. Bouchut, M. Farin, Continuum viscoplastic simulation of a granular column collapse on large slopes: μ(I) rheology and lateral wall effects, Phys. Fluids 29 (1) (2017) 013301, https://doi.org/10.1063/1.4971320.

[20] G.B. Crosta, S. Imposimato, D. Roddeman, Numerical modeling of 2-D granular step collapse on erodible and nonerodible surface, J. Geophys. Res., Earth Surf. 114 (F3) (2009) F03020, https://doi.org/10.1029/2008JF001186.

[21] C. Lusso, A. Ern, F. Bouchut, A. Mangeney, M. Farin, O. Roche, Two-dimensional simulation by regularization of free surface viscoplastic flows with Drucker–Prager yield stress and application to granular collapse, J. Comput. Phys. 333 (2017) 387–408, https://doi.org/10.1016/j.jcp.2016.12.036.

[22] S.B. Savage, K. Hutter, The motion of a finite mass of granular material down a rough incline, J. Fluid Mech. 199 (1989) 177–215, https://doi.org/10.1017/S0022112089000340.

[23] O. Pouliquen, Y. Forterre, Friction law for dense granular flows: application to the motion of a mass down a rough inclined plane, J. Fluid Mech. 453 (2002) 133–151, https://doi.org/10.1017/S0022112001006796.

[24] F. Bouchut, A. Mangeney-Castelnau, B. Perthame, J.-P. Vilotte, A new model of Saint Venant and Savage–Hutter type for gravity driven shallow water flows, C. R. Math. 336 (6) (2003) 531–536, https://doi.org/10.1016/s1631-073x(03)00117-1.

[25] F. Bouchut, M. Westdickenberg, Gravity driven shallow water models for arbitrary topography, Commun. Math. Sci. 2 (3) (2004) 359–389, https://doi.org/10.4310/CMS.2004.v2.n3.a2.

[26] R.R. Kerswell, Dam break with Coulomb friction: a model for granular slumping?, Phys. Fluids 17 (5) (2005) 057101, https://doi.org/10.1063/1.1870592.

[27] A. Mangeney-Castelnau, F. Bouchut, J.P. Vilotte, E. Lajeunesse, A. Aubertin, M. Pirulli, On the use of Saint Venant equations to simulate the spreading of a granular mass, J. Geophys. Res., Solid Earth 110 (B9) (2005) B09103, https://doi.org/10.1029/2004JB003161.

[28] A.N. Edwards, A.S. Russell, C.G. Johnson, J.M. Gray, Frictional hysteresis and particle deposition in granular free-surface flows, J. Fluid Mech. 875 (2019) 1058–1095, https://doi.org/10.1017/jfm.2019.517.

[29] P. Richard, A. Valance, J.-F. Métayer, P. Sanchez, J. Crassous, M. Louge, R. Delannay, Rheology of confined granular flows: scale invariance, glass transition, and friction weakening, Phys. Rev. Lett. 101 (24) (2008) 248002, https://doi.org/10.1103/PhysRevLett.101.248002.

[30] F. Radjaï, F. Dubois, Discrete-Element Modeling of Granular Materials, Wiley-Iste, Hoboken, New Jersey, USA, 2011, https://www.wiley.com/en-br/Discrete+element+Modeling+of+Granular+Materials-p-9781848212602.

[31] J. Estep, J. Dufek, Discrete element simulations of bed force anomalies due to force chains in dense granular flows, J. Volcanol. Geotherm. Res. 254 (2013) 108–117, https://doi.org/10.1016/j.jvolgeores.2012.12.023.

[32] F. Radjai, J.-N. Roux, A. Daouadji, Modeling granular materials: century-long research across scales, J. Eng. Mech. 143 (4) (2017) 04017002, https://doi.org/10.1061/(ASCE)EM.1943-7889.0001196.

[33] P.A. Cundall, O.D. Strack, A discrete numerical model for granular assemblies, Géotechnique 29 (1) (1979) 47–65, https://doi.org/10.1680/geot.1979.29.1.47.

[34] S. Luding, Introduction to discrete element methods, Eur. J. Environ. Civ. Eng. 12 (7–8) (2008) 785–826, https://doi.org/10.1080/19648189.2008.9693050.

[35] E. Corral, R.G. Moreno, M.J. García, C. Castejón, Nonlinear phenomena of contact in multibody systems dynamics: a review, Nonlinear Dyn. 104 (2) (2021) 1269–1295, https://doi.org/10.1007/s11071-021-06344-z.

[36] S.C. McNamara, Acoustics and frictional sliding in granular materials, Granul. Matter 17 (3) (2015) 311–324, https://doi.org/10.1007/s10035-015-0563-3.

[37] J.J. Moreau, P.D. Panagiotopoulos, G. Strang, Topics in Nonsmooth Mechanics, Birkhäuser Verlag, Basel, Switzerland, 1988, https://books.google.fr/books?id=9_NQAAAAMAAJ&redir_esc=y.

[38] J.J. Moreau, Unilateral contact and dry friction in finite freedom dynamics, in: J.J. Moreau, P.D. Panagiotopoulos (Eds.), Nonsmooth Mechanics and Applications, Springer, Vienna, 1988, pp. 1–82, https://link.springer.com/chapter/10.1007/978-3-7091-2624-0_1.

[39] M. Jean, J.J. Moreau, Unilaterality and dry friction in the dynamics of rigid body collections, in: Proceedings of the 1st Contact Mechanics International Symposium, Presses Polytechniques et Universitaires Romandes, Lausanne, Switzerland, 1992, pp. 31–48, https://hal.science/hal-01863710.
[40] J.J. Moreau, Some numerical methods in multibody dynamics: application to granular materials, Eur. J. Mech. A/Solids 13 (4) (1994) 93–114, https://hal.science/hal-01789082/.
[41] J. Moreau, Numerical aspects of the sweeping process, Comput. Methods Appl. Mech. Eng. 177 (3–4) (1999) 329–349, https://linkinghub.elsevier.com/retrieve/pii/S0045782598003879.
[42] M. Jean, The non-smooth contact dynamics method, Comput. Methods Appl. Mech. Eng. 177 (3–4) (1999) 235–257, https://doi.org/10.1016/S0045-7825(98)00383-1.
[43] J.J. Moreau, Modélisation et simulation de matériaux granulaires, in: B. Mohammadi (Ed.), Actes du 35e Congrès National d'Analyse Numérique, Online, La Grande Motte, 2003, pp. 1–30, https://hal.archives-ouvertes.fr/hal-01793668.
[44] D.E. Stewart, J.C. Trinkle, An implicit time-stepping scheme for rigid body dynamics with inelastic collisions and Coulomb friction, Int. J. Numer. Methods Eng. 39 (15) (1996) 2673–2691, https://doi.org/10.1002/(SICI)1097-0207(19960815)39:15<2673::AID-NME972>3.0.CO;2-I.
[45] D.E. Stewart, Rigid-body dynamics with friction and impact, SIAM Rev. 42 (1) (2000) 3–39, https://doi.org/10.1137/S0036144599360110.
[46] V. Acary, M. Brémond, O. Huber, On solving contact problems with Coulomb friction: formulations and numerical comparisons, in: R. Leine, V. Acary, O. Brüls (Eds.), Advanced Topics in Nonsmooth Dynamics, Springer International Publishing, Cham, 2018, pp. 375–457, http://link.springer.com/10.1007/978-3-319-75972-2_10.
[47] F. Radjai, V. Richefeu, Contact dynamics as a nonsmooth discrete element method, Mech. Mater. 41 (6) (2009) 715–728, https://doi.org/10.1016/j.mechmat.2009.01.028.
[48] L. Staron, E.J. Hinch, Study of the collapse of granular columns using two-dimensional discrete-grain simulation, J. Fluid Mech. 545 (2005) 1–27, https://doi.org/10.1017/S0022112005006415.
[49] L. Staron, E.J. Hinch, The spreading of a granular mass: role of grain properties and initial conditions, Granul. Matter 9 (3–4) (2007) 205, https://doi.org/10.1007/s10035-006-0033-z.
[50] V. Acary, F. Cadoux, C. Lemaréchal, J. Malick, A formulation of the linear discrete Coulomb friction problem via convex optimization, Z. Angew. Math. Mech. 91 (2) (2011) 155–175, https://doi.org/10.1002/zamm.201000073.
[51] M. Anitescu, Optimization-based simulation of nonsmooth rigid multibody dynamics, Math. Program. 105 (1) (2006) 113–143, https://doi.org/10.1007/s10107-005-0590-7.
[52] A. Tasora, D. Negrut, M. Anitescu, Large-scale parallel multi-body dynamics with frictional contact on the graphical processing unit, Proc. Inst. Mech. Eng., Proc., Part K, J. Multi-Body Dyn. 222 (4) (2008) 315–326.
[53] M. Anitescu, A. Tasora, An iterative approach for cone complementarity problems for nonsmooth dynamics, Comput. Optim. Appl. 47 (2) (2010) 207–235, https://doi.org/10.1007/s10589-008-9223-4.
[54] A. Tasora, M. Anitescu, A convex complementarity approach for simulating large granular flows, J. Comput. Nonlinear Dyn. 5 (3) (2010) 031004, https://doi.org/10.1115/1.4001371.
[55] A. Tasora, M. Anitescu, A matrix-free cone complementarity approach for solving large-scale, nonsmooth, rigid body dynamics, Comput. Methods Appl. Mech. Eng. 200 (5–8) (2011) 439–453, https://doi.org/10.1016/j.cma.2010.06.030.
[56] C. Petra, B. Gavrea, M. Anitescu, F. Potra, A computational study of the use of an optimization-based method for simulating large multibody systems, Optim. Methods Softw. 24 (6) (2009) 871–894, https://doi.org/10.1080/10556780902806094.
[57] K. Krabbenhoft, A.V. Lyamin, J. Huang, M. Vicente da Silva, Granular contact dynamics using mathematical programming methods, Comput. Geotech. 43 (2012) 165–176, https://doi.org/10.1016/j.compgeo.2012.02.006.
[58] T. Heyn, M. Anitescu, A. Tasora, D. Negrut, Using Krylov subspace and spectral methods for solving complementarity problems in many-body contact dynamics simulation, Int. J. Numer. Methods Eng. 95 (7) (2013) 541–561, https://doi.org/10.1002/nme.4513.
[59] H. Mazhar, T. Heyn, D. Negrut, A. Tasora, Using Nesterov's method to accelerate multibody dynamics with friction and contact, ACM Trans. Graph. 34 (3) (2015) 1–14, https://doi.org/10.1145/2735627.
[60] D. Melanz, L. Fang, P. Jayakumar, D. Negrut, A comparison of numerical methods for solving multibody dynamics problems with frictional contact modeled via differential variational inequalities, Comput. Methods Appl. Mech. Eng. 320 (2017) 668–693, https://doi.org/10.1016/j.cma.2017.03.010.
[61] E. Corona, D. Gorsich, P. Jayakumar, S. Veerapaneni, Tensor train accelerated solvers for nonsmooth rigid body dynamics, Appl. Mech. Rev. 71 (5) (2019) 050804, https://doi.org/10.1115/1.4043324.
[62] B. Maury, A time-stepping scheme for inelastic collisions, Numer. Math. 102 (4) (2006) 649–679, https://doi.org/10.1007/s00211-005-0666-6.
[63] A. Mangeney, O. Roche, O. Hungr, N. Mangold, G. Faccanoni, A. Lucas, Erosion and mobility in granular collapse over sloping beds, J. Geophys. Res., Earth Surf. 115 (F3) (2010) F03040, https://doi.org/10.1029/2009JF001462.
[64] M. Farin, A. Mangeney, O. Roche, Fundamental changes of granular flow dynamics, deposition, and erosion processes at high slope angles: insights from laboratory experiments, J. Geophys. Res., Earth Surf. 119 (3) (2014) 504–532, https://doi.org/10.1002/2013JF002750.
[65] S.J. Conway, A. Decaulne, M.R. Balme, J.B. Murray, M.C. Towner, A new approach to estimating hazard posed by debris flows in the Westfjords of Iceland, Geomorphology 114 (4) (2010) 556–572, https://doi.org/10.1016/j.geomorph.2009.08.015.
[66] R.M. Iverson, M.E. Reid, M. Logan, R.G. LaHusen, J.W. Godt, J.P. Griswold, Positive feedback and momentum growth during debris-flow entrainment of wet bed sediment, Nat. Geosci. 4 (2) (2011) 116–121, https://doi.org/10.1038/ngeo1040.
[67] R.M. Iverson, C. Ouyang, Entrainment of bed material by Earth-surface mass flows: review and reformulation of depth-integrated theory, Rev. Geophys. 53 (1) (2015) 27–58, https://doi.org/10.1002/2013RG000447.
[68] A. Mangeney, Landslide boost from entrainment, Nat. Geosci. 4 (2) (2011) 77–78, https://doi.org/10.1038/ngeo1077.
[69] G.J. Crutchley, J. Karstens, C. Berndt, P.J. Talling, S.F. Watt, M.E. Vardy, V. Hühnerbach, M. Urlaub, S. Sarkar, D. Klaeschen, M. Paulatto, A. Le Friant, E. Lebas, F. Maeno, Insights into the emplacement dynamics of volcanic landslides from high-resolution 3D seismic data acquired offshore Montserrat, Lesser Antilles, Mar. Geol. 335 (2013) 1–15, https://doi.org/10.1016/j.margeo.2012.10.004.
[70] O. Roche, Y. Niño, A. Mangeney, B. Brand, N. Pollock, G. Valentine, Dynamic pore-pressure variations induce substrate erosion by pyroclastic flows, Geology 41 (10) (2013) 1107–1110, https://doi.org/10.1130/G34668.1.
[71] G. Crosta, S. Imposimato, D. Roddeman, Numerical modelling of entrainment/deposition in rock and debris-avalanches, Eng. Geol. 109 (1–2) (2009) 135–145, https://doi.org/10.1016/j.enggeo.2008.10.004.
[72] A.N. Edwards, S. Viroulet, B.P. Kokelaar, J.M. Gray, Formation of levees, troughs and elevated channels by avalanches on erodible slopes, J. Fluid Mech. 823 (2017) 278–315, https://doi.org/10.1017/jfm.2017.309.
[73] S. Viroulet, A.N. Edwards, C.G. Johnson, B.P. Kokelaar, J.M. Gray, Shedding dynamics and mass exchange by dry granular waves flowing over erodible beds, Earth Planet. Sci. Lett. 523 (2019) 115700, https://doi.org/10.1016/j.epsl.2019.07.003.
[74] A.N. Edwards, S. Viroulet, C.G. Johnson, J.M. Gray, Erosion-deposition dynamics and long distance propagation of granular avalanches, J. Fluid Mech. 915 (2021) A9, https://doi.org/10.1017/jfm.2021.34.
[75] E.D. Fernández-Nieto, J. Garres-Díaz, A. Mangeney, G. Narbona-Reina, A multilayer shallow model for dry granular flows with the μ(I)-rheology: application to granular collapse on erodible beds, J. Fluid Mech. 798 (2016) 643–681, https://doi.org/10.1017/jfm.2016.333.
[76] C. Lusso, F. Bouchut, A. Ern, A. Mangeney, A free interface model for static/flowing dynamics in thin-layer flows of granular materials with yield: simple shear simulations and comparison with experiments, Appl. Sci. 7 (4) (2017) 386.

[77] E.D. Fernández-Nieto, J. Garres-Díaz, A. Mangeney, G. Narbona-Reina, 2D granular flows with the μ(I) rheology and side walls friction: a well-balanced multilayer discretization, J. Comput. Phys. 356 (2018) 192–219, https://doi.org/10.1016/j.jcp.2017.11.038.
[78] C. Kavinkumar, S. Sureka, R.J. Pillai, H. Mudavath, Influence of erodible layer on granular column collapse using discrete element analysis, Geomech. Geoengin. 17 (4) (2022) 1123–1135, https://doi.org/10.1080/17486025.2021.1928759.
[79] A.P.S. Mosek, The MOSEK optimization software, available at http://www.mosek.com. (Accessed 11 September 2023), 2010.
[80] S. De, E. Corona, P. Jayakumar, S. Veerapaneni, Scalable solvers for cone complementarity problems in frictional multibody dynamics, in: 2019 IEEE High Performance Extreme Computing Conference, HPEC 2019, 2019, pp. 1–7.
[81] M. Andersen, J. Dahl, Z. Liu, L. Vandenberghe, Interior-point methods for large-scale cone programming, in: S. Sra, S. Nowozin, S.J. Wright (Eds.), Optimization for Machine Learning, The MIT Press, Cambridge, USA, 2011, pp. 55–84, https://doi.org/10.7551/mitpress/8996.003.0005, https://direct.mit.edu/books/book/2929/chapter/79584/Interior-Point-Methods-for-Large-Scale-Cone.
[82] J.-B. Hiriart-Urruty, C. Lemaréchal, Convex Analysis and Minimization Algorithms I, Grundlehren der mathematischen Wissenschaften, vol. 305, Springer, Berlin, Heidelberg, 1993, http://link.springer.com/10.1007/978-3-662-02796-7.
[83] J. Kleinert, B. Simeon, M. Obermayr, An inexact interior point method for the large-scale simulation of granular material, Comput. Methods Appl. Mech. Eng. 278 (2014) 567–598, https://doi.org/10.1016/j.cma.2014.06.009.
[84] J. Kleinert, B. Simeon, K. Dreßler, Nonsmooth contact dynamics for the large-scale simulation of granular material, J. Comput. Appl. Math. 316 (2017) 345–357, https://doi.org/10.1016/j.cam.2016.09.037.
[85] A. Taboada, N. Estrada, F. Radjaï, Additive decomposition of shear strength in cohesive granular media from grain-scale interactions, Phys. Rev. Lett. 97 (9) (2006) 098302, https://doi.org/10.1103/PhysRevLett.97.098302.
[86] Engineering-ToolBox, Friction - friction coefficients and calculator, available at https://www.engineeringtoolbox.com/friction-coefficients-d_778.html. (Accessed 9 November 2023), 2004.
[87] H. Tang, R. Song, Y. Dong, X. Song, Measurement of restitution and friction coefficients for granular particles and discrete element simulation for the tests of glass beads, Materials 12 (19) (2019) 3170, https://doi.org/10.3390/ma12193170.
[88] H.A. Martin, M. Peruzzetto, S. Viroulet, A. Mangeney, P.-Y. Lagrée, S. Popinet, B. Maury, A. Lefebvre-Lepot, Y. Maday, F. Bouchut, Numerical simulations of granular dam break: comparison between discrete element, Navier-Stokes, and thin-layer models, Phys. Rev. E 108 (5) (2023) 054902, https://doi.org/10.1103/PhysRevE.108.054902.
[89] GDR-MiDi, On dense granular flows, Eur. Phys. J. E 14 (4) (2004) 341–365, https://doi.org/10.1140/epje/i2003-10153-0.
[90] A. Dufresne, Granular flow experiments on the interaction with stationary runout path materials and comparison to rock avalanche events, Earth Surf. Process. Landf. 37 (14) (2012) 1527–1541, https://doi.org/10.1002/esp.3296.
[91] F. Bouchut, E.D. Fernández-Nieto, E.H. Koné, A. Mangeney, G. Narbona-Reina, Dilatancy in dry granular flows with a compressible μ(I) rheology, J. Comput. Phys. 429 (2021) 110013, https://doi.org/10.1016/j.jcp.2020.110013.
[92] B. Cagnoli, A. Piersanti, Grain size and flow volume effects on granular flow mobility in numerical simulations: 3-D discrete element modeling of flows of angular rock fragments, J. Geophys. Res., Solid Earth 120 (4) (2015) 2350–2366, https://doi.org/10.1002/2014JB011729.
[93] E. Kermani, T. Qiu, T. Li, Simulation of collapse of granular columns using the discrete element method, Int. J. Geomech. 15 (6) (2015) 1–12, https://doi.org/10.1061/(ASCE)GM.1943-5622.0000467.
[94] F. Bouchut, I.R. Ionescu, A. Mangeney, An analytic approach for the evolution of the static/flowing interface in viscoplastic granular flows, Commun. Math. Sci. 14 (8) (2016) 2101–2126, https://doi.org/10.4310/CMS.2016.v14.n8.a2.
[95] L. Vanel, D. Howell, D. Clark, R.P. Behringer, E. Clément, Memories in sand: experimental tests of construction history on stress distributions under sandpiles, Phys. Rev. E 60 (5) (1999) R5040.
[96] V. Beatini, G. Royer-Carfagni, A. Tasora, A non-smooth-contact-dynamics analysis of Brunelleschi's cupola: an octagonal vault or a circular dome?, Meccanica 54 (3) (2019) 525–547, https://doi.org/10.1007/s11012-018-00934-9.
[97] PROJECTCHRONO, An open source multi-physics simulation engine, available at https://www.projectchrono.org. (Accessed 23 September 2022), 2018.